

# 1 Results

## 1.1 Tissue shape changes in evagination

### 1.1.1 Morphogenetic changes in the DP during evagination

To understand the morphogenetic changes in the DP during evagination, I used a single plane illumination microscopy (SPIM) imaging approach, which allows to acquire the full 3D shape at subcellular resolution with multi-angle imaging. I developed a pipeline for live wing disc dissections at larval and prepupal stages, followed by immediate mounting and imaging. This method allowed for *ex vivo* high-resolution imaging with an almost unperturbed, *in vivo* like, wing shape. To highlight the apical junctional network, a homozygous E-cadherin::GFP fly line was used and, for comparability to RNAi experiments, combined with a heterozygous nubbin-Gal4/+ driver. Each pupal disc was acquired in four angles to image dorsal, ventral, anterior-lateral, and posterior-lateral views. Each larval disc was acquired in three views as the dorsal and ventral half of the pouch are in the same plane at larval stages and they can be imaged in one view. For tissue shape analysis, a single 3D image was reconstructed from all views. I analyzed 5-7 discs per developmental stage; all subsequent tissue shape and cell shape analysis for wildtype wing discs in sections 1.1, 1.2, 1.3, and control in 1.4 is performed on the same set of wing discs (**TABLExx**).

Given the complexity of the 3D shape changes, I use a cross-section along the proximal-distal-axis, from notum to pouch (hereafter referred to as PD-crosssection/ PD-axis), and an apical surface projection of the wing disc to describe major morphological events (Figure 1-1 A-C). 3D volume views are available Supplemental movie 1\*\*\*

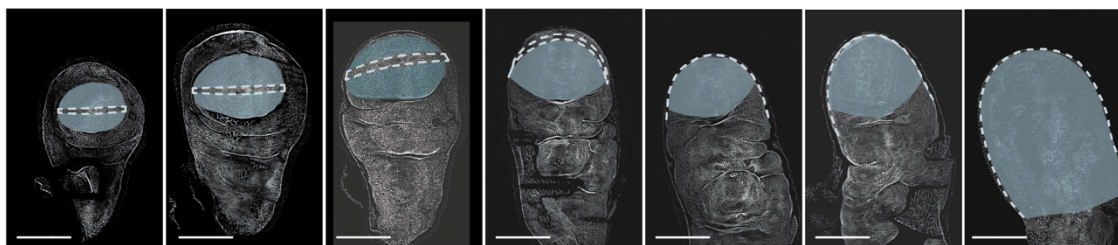
The subsequent analysis is done on two late larval growth stages: 96 hAEL (mid 3<sup>rd</sup> instar larvae), 120 hAEL (late 3<sup>rd</sup> instar larvae), and the last larval timepoint before puparium formation, at which the larva stops feeding and crawls out of the food: the so called wandering larval stage (wL3). I analyze 4 pre-pupal stages, which are staged from the timepoint of puparium formation: white Pupa (0 hAPF) and 2,4,6 hAPF stages.

Wing disc growth and fold has previously been studied in detail, however less attention has been given to the full 3D shape of the whole wing disc after the folds are initiated. Base on this dataset, wing disc shape at late developmental stages can be described as follows: At 96hAEL the three dorsal wing folds and one ventral fold can be observed, that is the continuation of the HP-fold surrounding the pouch. At 120 hAPF, the dorsal wing folds deepen and one additional ventral fold is formed. Moreover, the transition from DP to PE resembles a third fold. At wL3 the wing folds further deepen and the pouch becomes increasingly dome shaped (Figure 1-1 A, B).

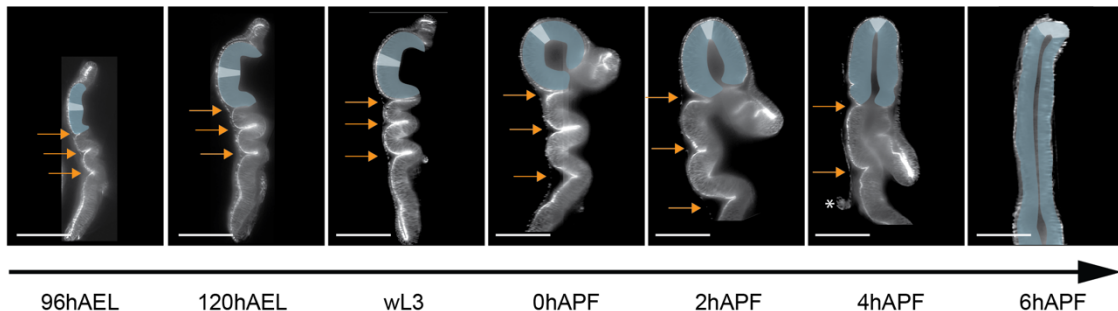
The tissue shape changes in eversion are characterized by the opening of the wing folds at the beginning of prepupal development. Opening starts at 0 hAPF and is almost complete with the removal of the PE at 4 hAPF. Additionally, the ventral wing folds open, so that the newly generated wing bilayer at 4 hAPF extends beyond the pouch region, ending at the hinge region between the HH and HN-fold. This dataset also confirms that the PE is removed around 4 hAPF (Pastor-Pareja et al., 2004). In 4 out of 7 analyzed 4 hAPF wing discs, the PE is opened up to the hinge region and in 3 discs it is removed entirely at 4 hAPF (Figure 1-1B).

At the same time the wing pouch changes its curvature: At eversion the pouch forms a bilayer, relocating the DV-boundary the distal most region of the wing disc, and flattening the curvature on the dorsal and ventral side. Tissue shape change at expansion if characterized by a decrease in apical basal cell height and tissue area expansion, which is more dramatic along the proximal distal (PD)-direction than along the anterior posterior (AP)-axis (Figure 1-1A, B).

A. Apical surface projection (disc proper)



B. Proximal-distal crosssection



96hAEL 120hAEL wL3 0hAPF 2hAPF 4hAPF 6hAPF

C. Schematics for 2D visualizations

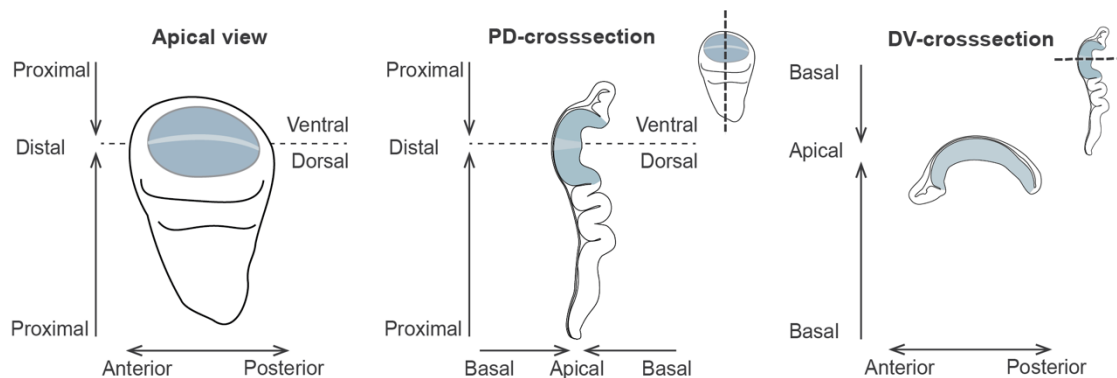


Figure 1-1 | Tissue shape changes during wing disc evagination

Tissue shape changes for developmental stages 96hAEL, 120hAEL, wL3, 0, 2, 4 and 6 hAPF. Representative examples out of 5-7 discs for each timepoint are chosen. Apical cell junctions are labelled with *Ecad::GFP* (A, B). Apical surface projection of the disc proper with the wing pouch highlighted in blue, the DV-boundary outlined with dashed lines (white) (A). Proximal distal crosssection along the center of the wing disc; the wing pouch is highlighted in blue, the DV-boundary in white and the positions of the three main wing folds are indicated with orange arrows (from top: HP-, HH-, HN-fold). The disc proper is overlayed by the thin peripodial epithelium (PE) from 96 hAPF to 4 hAPF; the asterisk at 4 hAPF indicates the opening part of the PE (B). Different 2D representations can be used to visualize tissue shape: Apical projection of the disc proper contains proximal-distal (PD), anterior-posterior (AP), and dorsal-ventral (DV) regional information. The PD-crosssection contains additional information of the apical-basal tissue height and apical curvature but loses information about changes along the AP-axis. The DV-crosssection shows apical curvature and tissue height changes along the DV-boundary in AP-direction, but has no PD-axis information. (C) Scalebars = 100 $\mu$ m

### 1.1.2 Pouch shape quantification

The pouch shape quantification was performed in collaboration with Abhijeet Krishna (MPI-CBG, CSBD and PoL). Abhijeet Krishna wrote the code for the mean shape generation from individual apical shapes and curvature measurements. (MM)

I subsequently focused my analysis on the tissue shape changes in the wing pouch, using a cross-section along the PD-axis and a DV-boundary cross-section (Figure 1-2 A, B). Mean pouch shapes are generated for the apical side along both directions, covering the pouch region up to the HP-fold.

The data show that the total apical distance between HP-folds at 96 hAPF is similar along the PD- and DV-axis, however as larval growth continues the shapes of the PD- and DV-axis become increasingly different. The PD-axis becomes more curved upon entering the folds, while the DV-boundary generally follows a wider arc. The shape anisotropy is maintained throughout eversion and expansion (Figure 1-2 C).

These observations can be quantified by measuring curvature changes along the apical outline. During all larval stages, the curvature of the wing pouch is similar in the center of the pouch for the DV- and PD direction, but it is different towards the fold region (Figure 1-2 D). In the center of the pouch at 96 hAEL, tissue curvature is close to 0 and throughout larval stages, the pouch remains flatter in the center than in the periphery. Thus, curvature increases when going away from the center along both directions. The curvature in the pouch is generally higher along the PD direction and approaches 0, when entering the folds. Overall, during larval growth, the curvature increases in the center of the disc giving rise to an increased dome shape that is inhomogeneous along the PD- and DV-axes (Figure 1-2 D).

During eversion, the curvature along the PD axis increases more than 2-fold in the center of the disc leading to a reversal of the curvature profile as compared to the late larval stage. By the end of eversion, at 4 hAPF, the curvature along the PD axis is increased by  $0.01 \mu\text{m}^2$  in the center of the pouch and approaches 0 in proximal part of the pouch, while the curvature increase along the DV-boundary is less dramatic. During expansion from 4 hAPF to 6 hAPF, the pouch undergoes an even more dramatic curvature increase along the PD-axis by 4-fold, from  $0.015$  to  $0.06 \mu\text{m}^2$ , while the curvature along the DV-boundary does not change (95% confidence interval of the mean) (Figure 1-2 D).

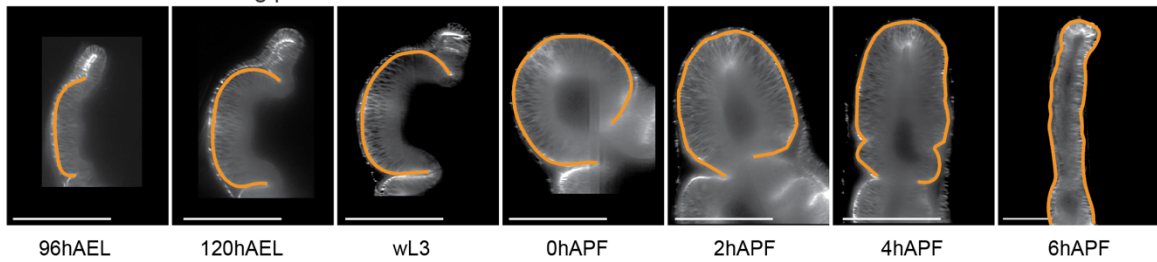
### 1.1.3 Spatial changes in tissue height during morphogenesis

I approximated Tissue height by finding the closest basal point for each position along the apical side of the pouch. The height profiles are averaged between anterior and posterior side for the DV-Boundary, and dorsal and ventral side for the PD direction and displayed from pouch center to the periphery (Figure 1-2 E).

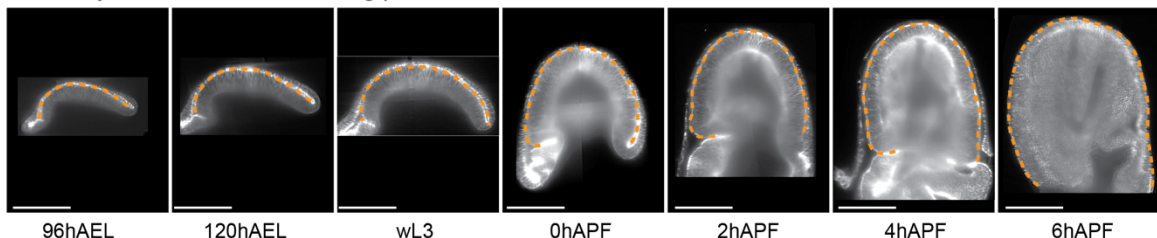
Similar to curvature, tissue height changes dynamically across growth and evagination.

Tissue Height increases during larval growth, while remaining higher in the center than in the periphery. Up to 50  $\mu\text{m}$  from the center, tissue height is similar between the DV and PD axis at larval stages. During eversion and expansion, tissue height in the DV boundary decreases dramatically and becomes isotropic along the DV axis. Along the PD axis the height gradient reverses, the tissue is slightly flatter in the center than in the periphery, until the tissue enters the HP-fold, where it flattens again. The most dramatic height decrease is observed during expansion (6 hAPF), reducing the tissue height to 50-60% of the height from 4 hAPF (Figure 1-2 E).

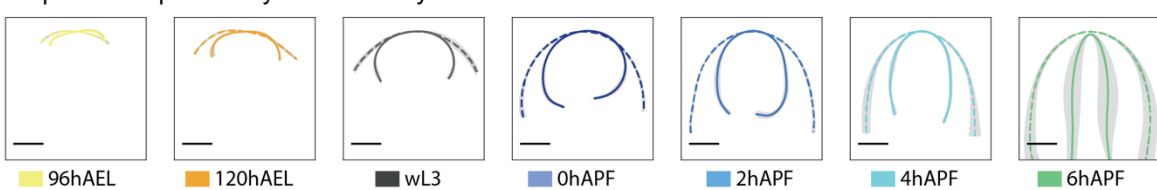
A. PD crosssection of the wing pouch



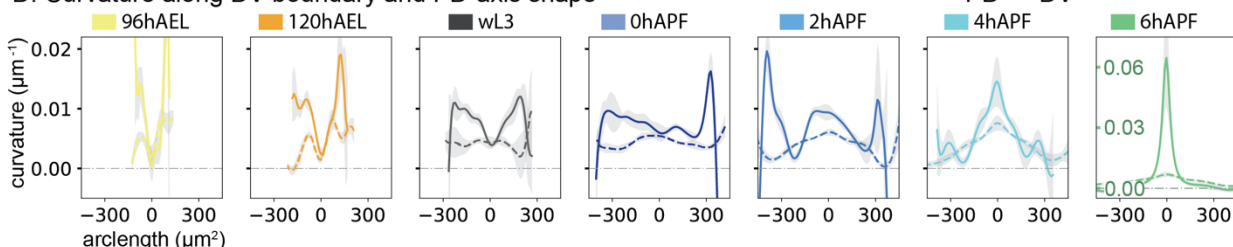
B. DV-boundary crosssection of the wing pouch



C. Apical pouch shape overlay DV-boundary and PD-axis



D. Curvature along DV-boundary and PD-axis shape



E. Apical-basal distance (tissue height (μm)) along DV-boundary and PD-axis

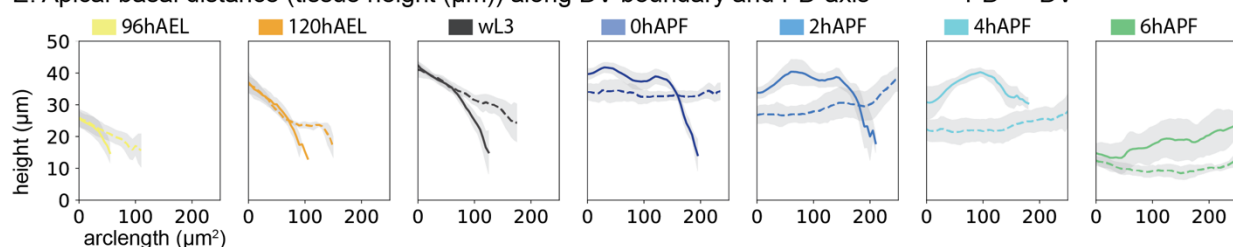


Figure 1-2 | Shape and curvature quantification in the wing pouch

Outline of apical tissue shape in the wing pouch along the PD-crosssection and along the DV-boundary crosssection for developmental stages 96hAEL, 120hAEL, wL3, 0 ,2 ,4 and 6 hAPF. Apical cell junctions are labelled with Ecad::GFP (A, B). Plot in A-E: DV = dashed line, PD = solid line. Mean shape curves for all stages and all discs analyzed along DV- and PD-axis; the center of the pouch is facing up, dorsal is left and ventral right in case of the PD-cross-section, and anterior is left for the DV-boundary cross-section; grey region indicates the 95% confidence interval of the mean for x and y position (C). Curvature quantification (in  $\mu\text{m}^{-1}$ ) along the apical shape by arclength, grey region indicates the 95% confidence interval of the mean for the curvature, y-axis from -0.005 to 0.022  $\mu\text{m}^{-1}$  for all stages except 6 hAPF, where the y-axis is indicated on the plot (D). Tissue height quantifications from center to out, tissue height ( $\mu\text{m}$ ) between dorsal-ventral and anterior-posterior axis are averaged on the distal-most part of the pouch (the center of the arc). Grey region indicates the 95% confidence interval of the height . The region of the DV-boundary that corresponds to the PD-axis, is at the center of the DV-axis, and thus included in the DV-axis plot at small arclength. This region has been excluded from the PD-axis for these plots (E). Scalebars = 100 $\mu\text{m}$

#### 1.1.4 Summary tissue shape changes during evagination

I established a workflow for multi-view acquisition and 3D reconstruction of live wing imaginal disc during growth, eversion and expansion. This dataset offers an unprecedented level of detail and insight on tissue shape changes during these morphogenetic processes. I observe temporal kinetics of fold deepening from 96 hAEL to wL3 stage, followed by unfolding during eversion. The wing pouch becomes increasingly domed during growth, but even more so at wL3 stages and changes its curvature thereafter to accomplish the formation of the wing bilayer.

I then focus tissue shape analysis further on the wing pouch: Overall, the quantification of curvature changes reveals a shape anisotropy along DV- and PD-axes. Curvature changes are spatially and temporally inhomogeneous, yet throughout growth and evagination the tissue gradually increases its curvature at the distal most point and flattens in the proximal regions that will give rise to the wing blade. The shape anisotropy is in accordance with going from a dome like shape to a bilayer. Interestingly, the curvature dynamics along the DV-axis are less dramatic as compared to the changes along the PD-axis.

Previous research has described tissue area expansion by apical-basal flattening from 4 to 7 hAPF (Diaz-de-la-Loza et al., 2018). Diaz-de-la-Loza et al., also observe anisotropy of expansion, the future wing blade elongates along the PD-axis but does not increase in width between 4 hAPF to 6 hAPF. My observations on tissue height changes and shape anisotropy are in accordance with these results.

In order to understand local morphogenetic changes, tissue shape needs to be compared regionally. Yet, due to potential tissue expansion by cell shape changes and topology changes, regional changes in curvature cannot be simply compared by position along the arclength. Instead, a more precise spatial mapping that takes tissue expansion due to cellular behavior into account is required

## 1.2 A topological method for spatial analysis

The development of a computational method for 3D apical cell shape analysis as an extension of Tissue Miner was done in collaboration with Joris Pajjmans, Charlie Duclut and Marko Popović. The code relevant for this thesis and individual contributions are indicated in the Materials and Methods.

### 1.2.1 Extracting cell shape information for curved surfaces

The observed inhomogeneity of tissue shape changes necessitates spatial-temporal mapping of cell and tissue properties over development. Typically, such an approach would involve 4D live imaging of a developmental time series and tracking of cell and tissue movements (Etournay et al., 2016). However, although it is possible to live image wing disc eversion *ex vivo* in a tissue culture system, such an approach comes with limitations for full 3D live imaging, potential side effects of culturing, and effects on tissue shape due to external confinement necessary for imaging (Aldaz et al., 2010; Dye et al., 2017) Figure 1-3.

Supplementary movie XXX.

Live imaging of wing disc evagination

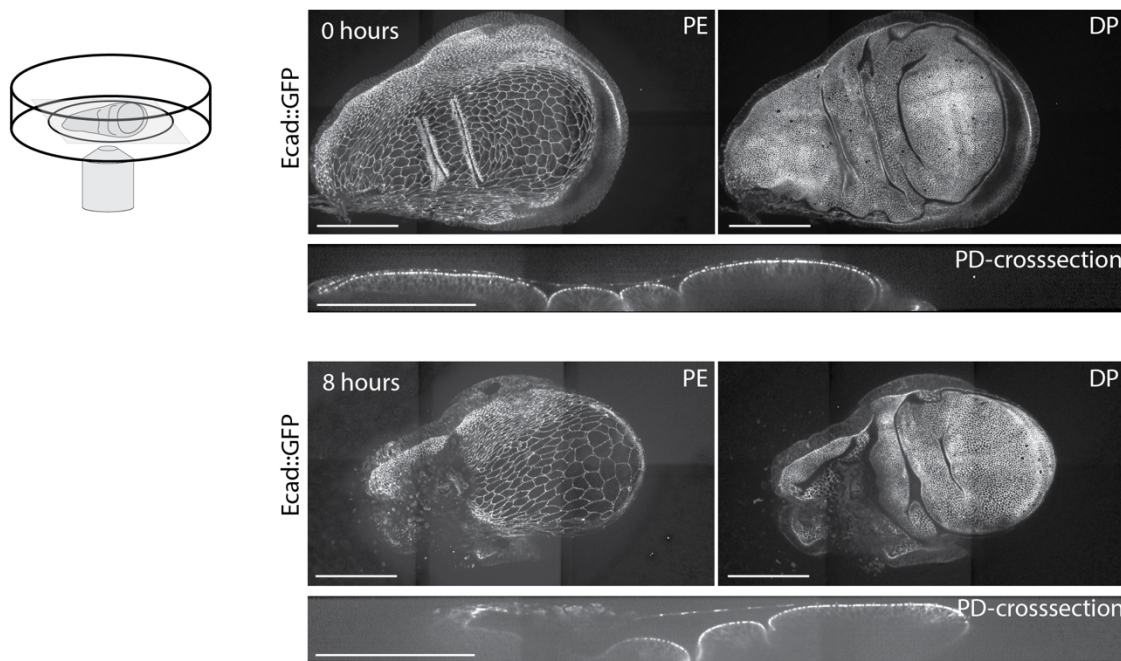
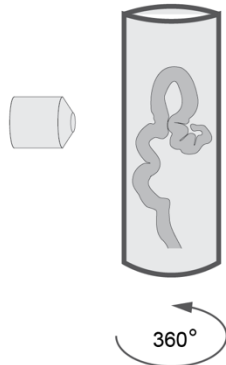


Figure 1-3 | Confocal live imaging provides only partial information on cell and tissue shape

Wing disc eversion in culture in combination with spinning disc confocal live imaging. Wing discs are dissected and mounted at wL3 stage; culture medium contains 400nM of 20E for eversion. Snapshots show apical surface projection of DP and PE and a crosssection view along the PD axis. Images show 0 and 8 hours of imaging, of a 14 hours movie with 5 min intervals, signal = Ecadherin::GFP

Given these limitations, I decided to explore the static, but full 3D dataset we use for tissue shape description that allowed *in vivo* development until the time of imaging. In order to get cell shape information, I project the apical surface of the DP and segment cell shapes in the wing pouch as described previously (Aigouy et al., 2016; Dye et al., 2017). Note that for pupal stages we segment cell shapes on each imaging angle separately instead of using a full 3D multiangle fusion approach as we do for tissue shape analysis. This is necessary as multi-angle imaging takes 2-5 minutes and during that time period the tissue moves slightly and cell shapes fluctuate which impacts on the image resolution and the ability to segment cell shapes in multi-angle reconstructed images. Moreover, cell shapes are segmented on a 2D projection, thus cells shape in highly folded regions is not resolvable (Dye et al., 2017).

A. Multi-angle SPIM imaging setup



B. DP surface projection for 90° angles at 2hAPF

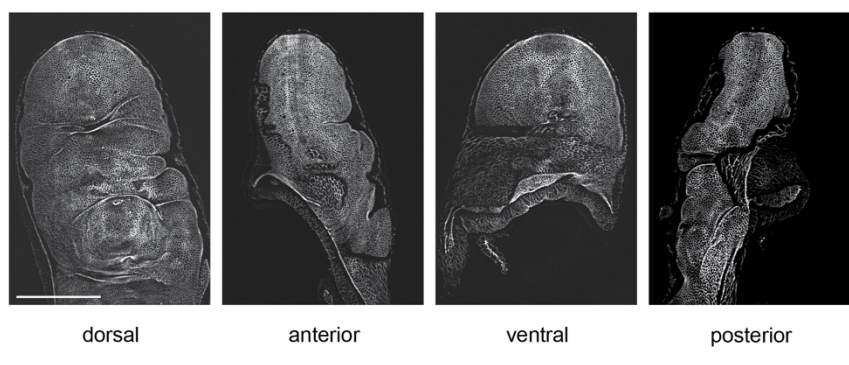


Figure 1-4 Multi-angle SPIM setup captures the tissue surface except for folded regions  
Schematics, showing the imaging setup for live wing discs in 1% low melting agarose. The agarose column is rotated for multi-angle imaging (A). DP surface projections for dorsal, ventral and lateral imaging angles on a 2 hAPF wing disc. Scale bar = 100  $\mu$ m

Next, I extract cell shape information from the segmentation mask and use the height maps from the surface projection to gain 3D position of cell vertices (Figure 1-5 A). This method has been developed in collaboration with Joris Pajmans and takes tissue curvature into account. This advances the previously established 2D analysis of cell and tissue shape, generating a curved surface description of tissue shape. This method is generally applicable to any curved surface analysis, if heightmaps generated from the 2D projection of the segmented tissue are available.

### 1.2.2 Establishing topological coordinate systems

To spatially map different regions in the tissue I make use of morphological landmarks and compartment boundaries that are identifiable by E-cadherin::eGFP (E-cad::eGFP) on apical cell junctions. Morphological landmarks that are easy to define throughout growth and evagination are the dorsal and ventral half of the wing blade, the DV-boundary, the PD-axis and often the AP-axis (Figure 1-1 C). Other well established morphological landmarks involve the future wing veins, the AP-boundary or the dorsal sensory organ precursors, however none of these are identifiable on apical cell morphology throughout all evagination stages.

Previous analysis of cell shapes in the wing disc have revealed a radial pattern of cellular properties that is centered at the distal tip of the pouch (Dye et al., 2021). Together with the fact that there are no cell flows across the DV-boundary, this makes the distal tip a suitable candidate for orienting a regional analysis of cell and tissue shape changes. Another such candidate could be the DV-boundary itself, which has however more complex changes in the spatial coordinates over time.

In order to achieve a spatial binning by a polar coordinate system around the distal tip, I use a spatial binning method based on the topological distance in the tissue. Here, the unit of distance is the number of cells on the shortest path between two points, where the path connects through shared bonds between cells, or in other words – cell neighbors (Figure 1-5 B, C).

This has the advantage, as compared to metric distance, that it is independent of 3D tissue shape. Moreover, A topological method is robust to cell shape changes as they do not directly affect the neighborhood relationship in the Tissue. Yet, it is still sensitive to topological changes, such as cell rearrangements, death or division.

During wing disc growth, cell rearrangements occur approximately at a rate of  $1.0 \text{ cell}^{-1}\text{hr}^{-1}$ . If the rearrangement frequency is similar though subsequent stages, per time interval of 2 hr (our analysis), cells would remain within 0-2 cells distance from their original cellular neighborhood. Another aspect that can change the topological position are cell death and cell division, yet as the wing disc enters a phase of growth arrest at late larval stages, we assume for the analysis of evagination, that those contributions do not lead to a dramatic change in topology or cell number. For the analysis of cell shape change during growth this assumption does not hold true. However, the growth process has been studied previously in detail and the focus of this work lies

on the studies of evagination. Growth stages will only be included for completeness, when necessary to understand subsequent morphogenesis.

In order to establish polar coordinates, the tissue center of the wing disc needs to be identified. As indicated above, different morphological landmarks are suitable spatial analysis. Moreover, the wing pouch can be morphologically subdivided into 2 main regions: the DV-boundary and the pouch outside the DV-boundary. The DV-boundary, a mechanically and morphologically distinct long stripe of cells, that bends during morphogenesis along its long axis, but remains rather flat along its short axis. The DV-boundary is subdividing the dorsal and ventral half of the wing pouch, which start out as two halves of a hemispherical cap at larval stages and flatten successively.

Each of those regions gets assigned a center, from which a topological spatial coordinate system is established. As dorsal and ventral side of the pouch are imaged in different views, I define the tissue center for dorsal and ventral half separately. Thereafter, dorsal and ventral half are considered symmetrical and cell and tissue shape properties are averaged over both sides. This is motivated by the observation that tissue curvature changes along both sides are similar, thus any properties that contribute to shape should be observed in both regions simultaneously and a merge of these regions reduces analysis noise. Dorsal and ventral pouch combined will be called outDV region hereafter.

As the tissue center is not identifiable unambiguously by eye, for dorsal and ventral pouch regions, first the cells at the edge of the segmentation mask that are facing the HP-fold are identified (margin region) Next, the shortest topological distance to the margin for every cell in the tissue is calculated (Figure 1-5 B). This results in a spatial binning that is non-radial and depends on the segmented region and the margin shape but it identifies the cells furthest away from the margin (at maximum  $k$ ), which are then used to define one center cell. The identified center cell is used to initiate the radial topological distance metric, leading to a radial spatial binning by  $k$  (Figure 1-5 C and D). In relation to the polar coordinate system, the radius  $r$ , is resembled by topological distance  $k$ , and the angle  $\varphi$  is orthogonal to  $r$ . Cells within the same topological distance to the center (topological ring) have the same  $r$  but different  $\varphi$ .

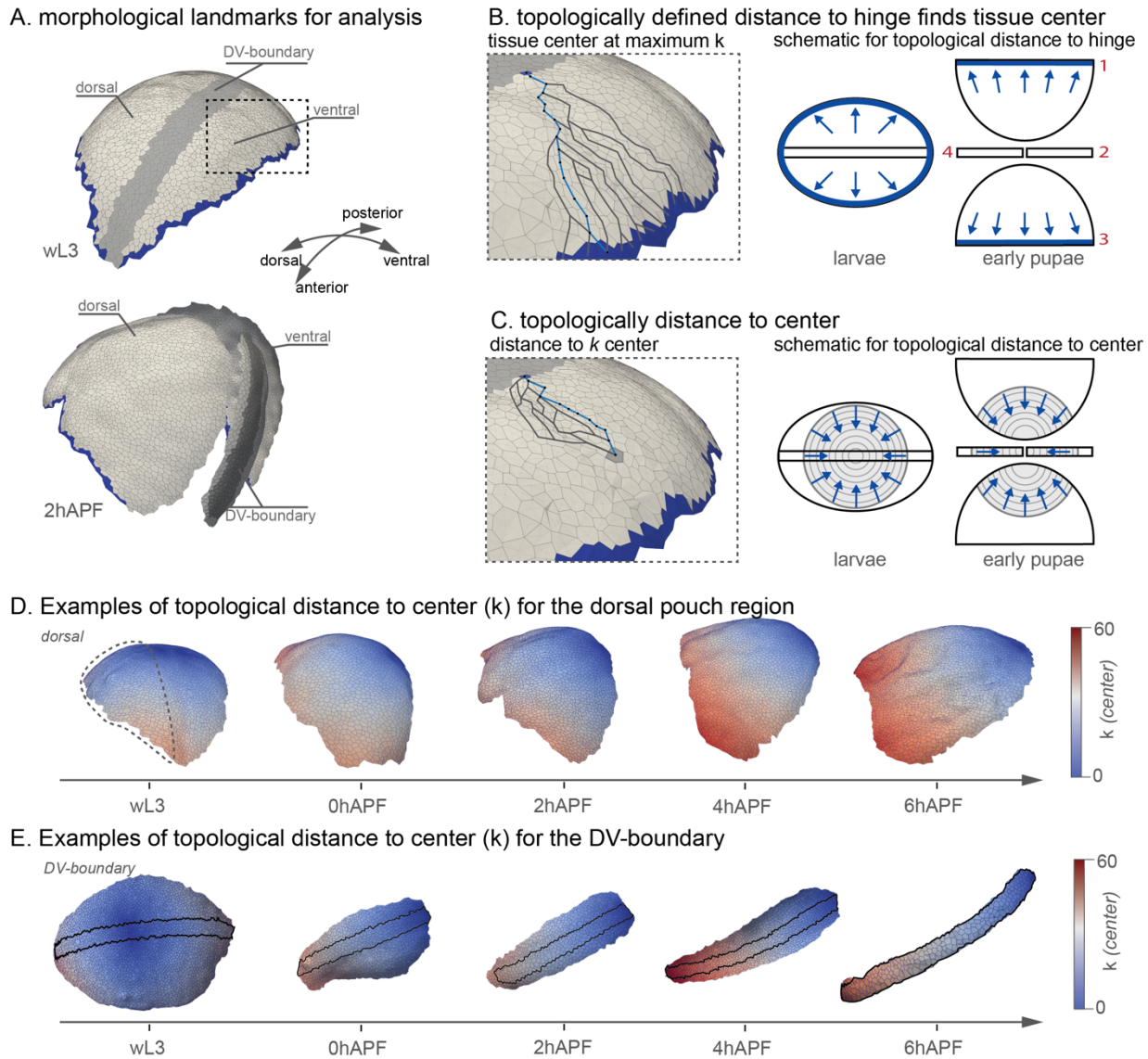


**Figure 1-5| A topological method for spatial analysis**

3D visualization of a segmented larval (wL3) and early pupal (2 hAPF) wing pouch. The larval pouch can be segmented in one view, as dorsal and ventral and DV-boundary live in the same plane, the pupal pouch is segmented in 4 views due to its double-layer structure. Morphological landmarks can be identified by eye. The region, facing the HP-fold is given by Tissue Miner (margin cells) without an overlay with DV-boundary neighbors (A). We find for each cell in the tissue its shortest topological distance to the margin (B). To do so, paths to all margin cells are calculated. One cell can have multiple equally shortest paths. We show examples of a few potential topological paths and highlight the shortest in blue (B). The shape of the so-generated topological bins method highly depends on the tissue outline. To get to a radial approximation, we find the center with the longest topological path to the HP-fold, and count the reverse, the shortest topological path to the center. We highlight in blue the shortest path to the center from an arbitrary chosen cell in the tissue (C). D and E show examples of this spatial topological distance (k), for the dorsal tissue and the DV-boundary for developmental stages over evagination.

For the DV boundary a slightly different approach is used, as the DV boundary is only a few cells wide and resembles more a cartesian geometry with the x-axis along, and the y-axis across the DV-boundary. (Figure 1-5 E). To approximate a cartesian geometry, a stripe of cells is defined as center. This is defined for larval stages as the DV-boundary cells between  $k = 0$  for dorsal and ventral and for pupal stages by the cells facing the tissue margin distally. (MM)

Taken together, wing disc evagination presents 4 different analysis challenges: larval and pupal stages, that are inherently different on the number of images necessary to get the full pouch shape, and the different regions, DV-boundary and the outDV region, follow different geometrical logic.

For comparability between timepoints we further apply a set of rules that defines a region tracked by topological distance to the center (Figure 1-6).

1. The number of cells for analysis is given by the number of cells in the wL3 stage and is contained for subsequent timepoints.
2. Topological bins cannot be discontinuous
3. Center cells for dorsal and ventral half of the outDV region are defined by the maximum distance to the margin region. The margin region is defined for larval stages to be the cells at the edge of the segmentation mask, excluding cells from the DV-boundary. For pupal stages, as the DV-boundary is not in view, I exclude those cells next to the DV-boundary.
4. The center cells for the DV-boundary at larval stages are given by their metric position in the disc. Lying on a path between the center cells of the dorsal and ventral half.
5. Center cells for the DV-boundary at pupal stages are given by tissue orientation, overlap with the tissue margin and the DV-boundary.

### Establishing a topological coordinate system for all possible tissue geometries

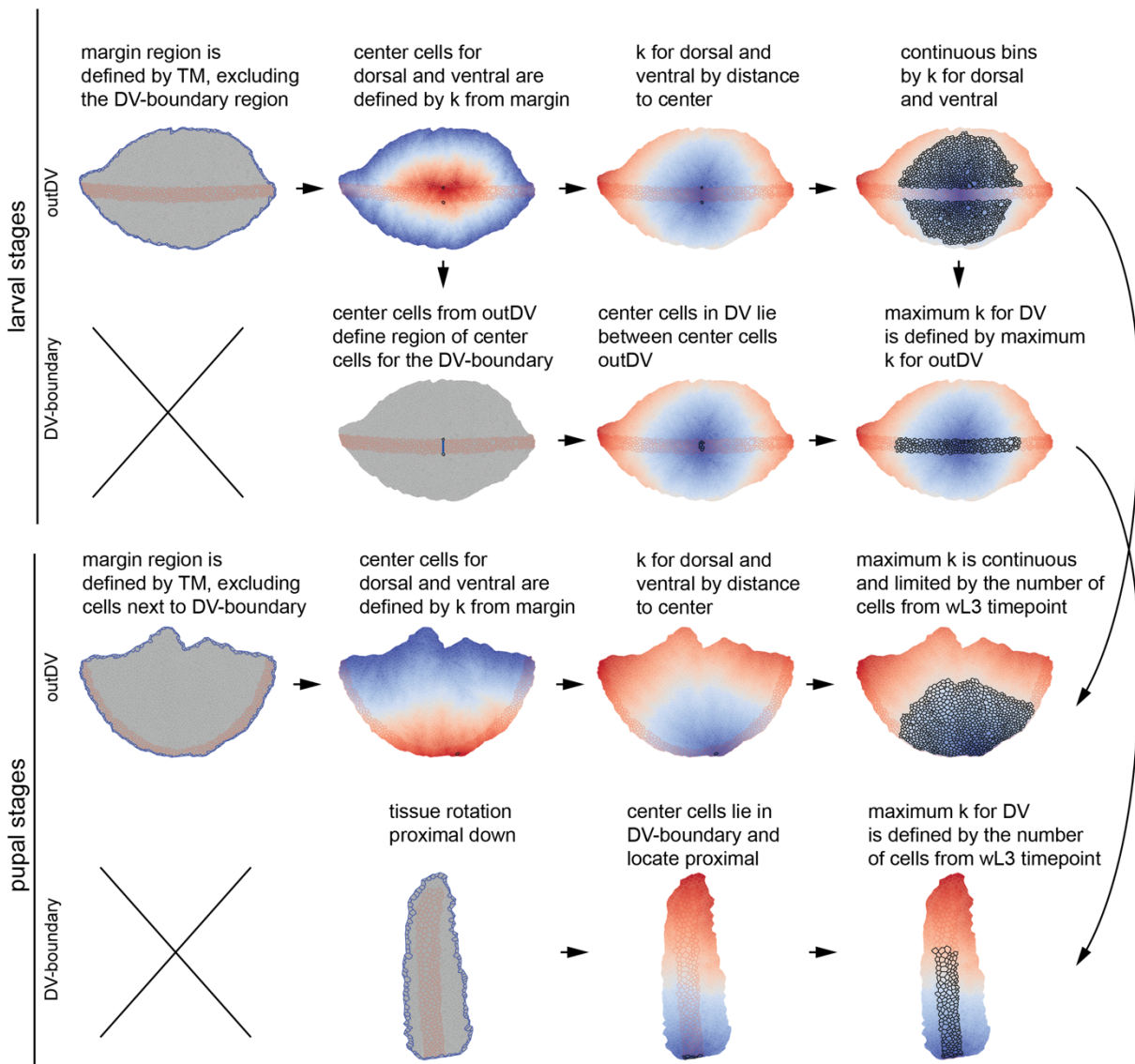


Figure 1-6 | Overview of topological coordinates workflow

We present the workflow for on exemplary images for larval (wL30 and pupal (2 hAPF) stages.  $k$  distance is indicated by cell color from blue to red. blue = small  $k$ , red = large  $k$ . Cell bonds of cells from the margin region are outlined in blue, cell bonds from cells in the DV-boundary (for larva: outDV, DV-boundary and pupa: DV-boundary views) or next to the DV-boundary (pupa: outDV region) are outlined in red. Center cells are highlighted in black for the second and third column and all cells included in the analysis are highlighted in black for the fourth column.

Using the topological distance method, cells with the same topological distance to the center can be coarse grained into one bin, this leads to a 1D description by distance, but not by the second coordinate axis, which represents the width (or the y-axis) in case of the DV-boundary or the angle ( $\phi$ ) for the outDV region. I make this assumption since a radial dependency of cell properties has been demonstrated before and I am following a coarse-grained approach by comparing developmental stages that are relatively far apart. However, a second topological distance can be introduced, when necessary, to generate a 2D coordinate system and unambiguous spatial topological coordinates for each cell. The advantage of a topological coordinate system as compared to a metric system is its versatility, and tissue shape and curvature independence. Moreover, we can use it as a tool to establish topological distance and cell number based relationships between different timepoints.

### 1.2.3 Spatio-temporal mapping of cells and tissue shape by topological relationships

The relationships of topological distances between timepoints were established in collaboration with Abhijeet Krishna

Topological binning reveals that I segment larger tissue areas with increasing topological distances from the center during eversion, which can be explained by those cells that were previously hidden in the HP-fold coming into view as the fold opens up. To understand tissue and cell shape changes during eversion, analysis needs to be limited on the region that is visible over all timepoints and has not been hidden in the folds at larval stages. Moreover, as I use radial binning, and average out angular effects, only those topological bins that are uninterrupted along their tangential axis, within the outDV region, can be included in order to be consistent on the effect of averaging. This excludes the outermost topological rings that intersect with the fold region. We then use the cumulative number of cells from the reference timepoint wL3 to identify the matching regions at later stages based on the number of cells (Figure 1-6). In order to keep the number of cells constant, the maximum topological distance must increase from 21 to 24 in the outDV region and from 21 to 37 in the DV boundary (Figure 1-7 A). These changes can be explained by changes in tissue topology, such as cell rearrangements, during eversion. Although the unit of measurement for  $k$  is the number of cells, the path length, connecting cell centers, can be calculated in  $\mu\text{m}$  distance. This calculation reveals, that within the same topological

distance, the metric ( $\mu\text{m}$ ) distance from the center increases during eversion and expansion. revealing that on top of topological changes, cell shape changes are happening during both processes (Figure 1-7 C). To be able to spatially compare cell shapes we use the relationship between cell number and topological distance  $k$  to establish a  $K_{ref}$  based spatial measurement, where  $K_{ref}$  is determined by the topological bin of the reference timepoint ( $k_{initial}$ ) and uses  $N(k)$ , which is the cell number per  $k$ , to make a weighted average of the corresponding topological bins for the timepoint to compare ( $k_{final}$ ) (Figure 1-7 B).

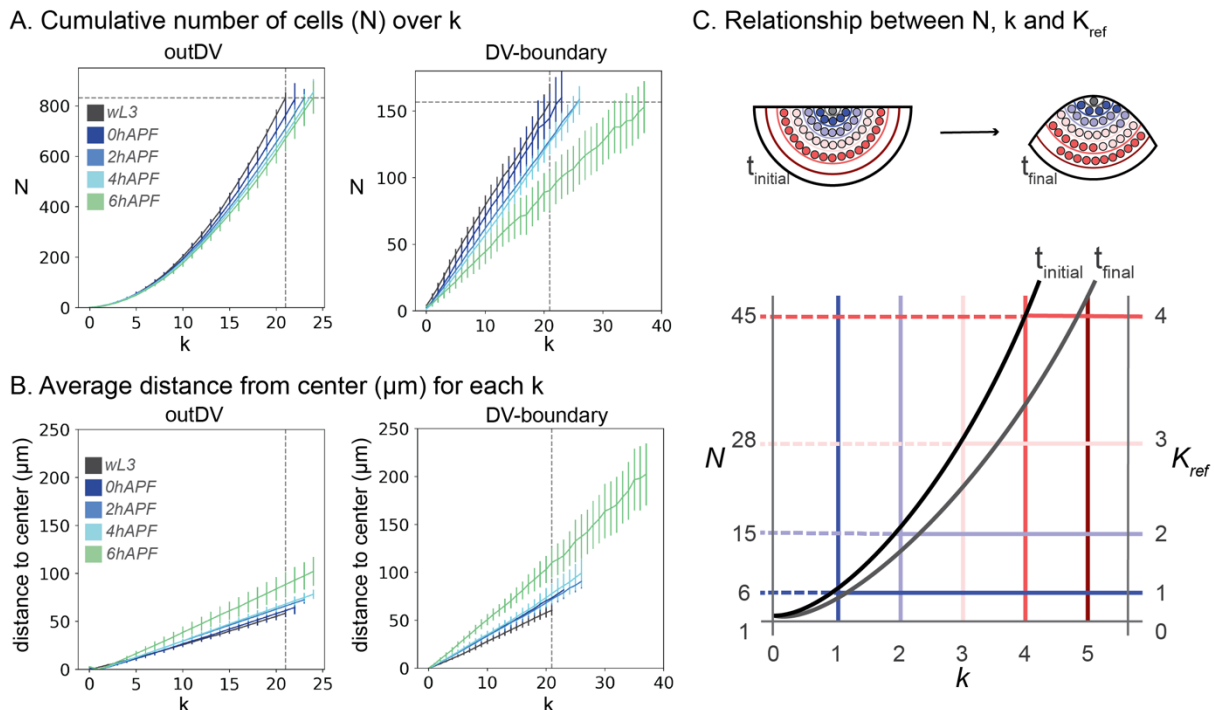


Figure 1-7 | Comparing topological coordinates between timepoints

Analysis of the relationship between  $k$ , the cumulative number of cells ( $N$ ) and distance in  $\mu\text{m}$ . As  $k$  increases, the number of cells contained up to  $k$  ( $N(k)$ ) also increase (A). We calculate the distance to  $k=0$  for each cell and average by topological bin (B). DV-boundary and outDV are plotted separately, different developmental stages are indicated by color, the vertical dashed line shows the average  $N$  at maximum  $k$  for wL3, the horizontal dashed line shows maximum  $k$  for wL3 in the respective region. Error bars indicate the 95% confidence interval of the mean (A, C). The relationship between  $N$  and  $k$  is given for each timepoint. To compare spatial properties between timepoints we set  $K_{ref}$  based on  $N(k)$  of the initial, or reference timepoint and use a  $K_{ref}$  based spatial binning which consist of a weighted average of  $k$  by  $N(k)$  for the final timepoint. For the initial timepoint,  $N(k_3) = 28$  cells and  $K_{ref} = k_3$ , for the final timepoint, we keep  $N = 28$ , yet to achieve this number of cells we are including a half of the next topological bin ( $k_4$ ) and  $K_{ref} = k_3 + \frac{1}{2}k_4$

#### 1.2.4 Applying spatial information to tissue shape analysis

Until now I analyzed tissue shape and curvature changes on the full pouch region. Yet in order to understand the interplay between cell and tissue shape changes, tissue shape the analysis needs to focused on the region of the pouch, where I have information on cell shapes over all timepoints. As seen above the topologically defined region can also be measured by distance in  $\mu\text{m}$  form the tissue center. Using this metric distance approximation for topological tissue patches, the tissue shape analysis can be refined to a region where I obtained cell shape information throughout all developmental stages (Figure 1-8 A).

Here I need to make a methodological distinction between growth and evagination stages: For evagination stages (wL3 to 6 hAPF) I use the average distance at maximum  $K_{ref}$  to compare tissue shape changes over developmental time. As this  $K_{ref}$  is only valid for developmental processes with no net growth, it cannot be used comparison between larval stages, when the tissue is still growing. Yet, previous analysis during wing disc growth at 96hAEL has shown that tissue growth and cell divisions are homogeneous throughout the pouch (Dye et al., 2021). As cell shapes are only segmented in the homogeneously growing region of the pouch, this region can be used for comparative analysis. Thus, for growth stages, a comparison over the segmented region without restrictions on cell number and topological distance is reasonable. Under this assumption, I use the maximum distance at the respective maximum  $k$  for all timepoints to define the region along the tissue shape that is contained by cell shape analysis.

I observed, that that the topologically tracked region only constitutes a small part of the pouch region. This is on one hand due to our rigorous exclusion of discontinuous topological bins at the larval stages, and on the other hand indicates a big contribution by cells derived from the HP-fold during evagination stages (Figure 1-8 A). A region that I cannot segment during larval stages and thus need to exclude from the analysis.

For the subsequent analysis, and in the region, we analyze, the three main developmental processes are characterized as follows (Figure 1-8 B,C):

At the transition from larval growth to wL3 stage, the top of the pouch becomes increasingly dome shaped. The curvature remains higher along the PD-axis towards the folds. The curvature at the wL3 stage is spatially homogenous along the DV-axis, resembling a spherical cap. Along the

PD-axis the curvature in the center matches the one in the DV-axis but it becomes more curved towards the periphery.

At eversion, the curvature increases dramatically at the center of the PD-crosssection, which corresponds the tissue region close to, and across, the DV-boundary. The curvature increase along the DV-boundary is more subtle.

At expansion, the curvature increased even further across the DV-boundary, and we do not observe changes along the DV-boundary.

Some of the features observed on the full pouch shape analysis will not be immediately addressed, as they lie outside the topologically defined region. Yet they offer interesting questions on tissue morphogenesis:

For late eversion and expansion stages, the pouch reached zero curvature on the outDV region, this regime is outside the topologically confined region and I will not further consider it in this analysis. Nevertheless, cell shape information for this region is available and might offer information on the transition form of curved to flat epithelial sheets.

Moreover, the high tissue curvature for larval stages, at the beginning of the folds, is not covered by the topologically defined region. The folds for in larval stages could lead to interesting observations on cell packing geometry, on a small radius of curvature for apical-outwards bend tissues.

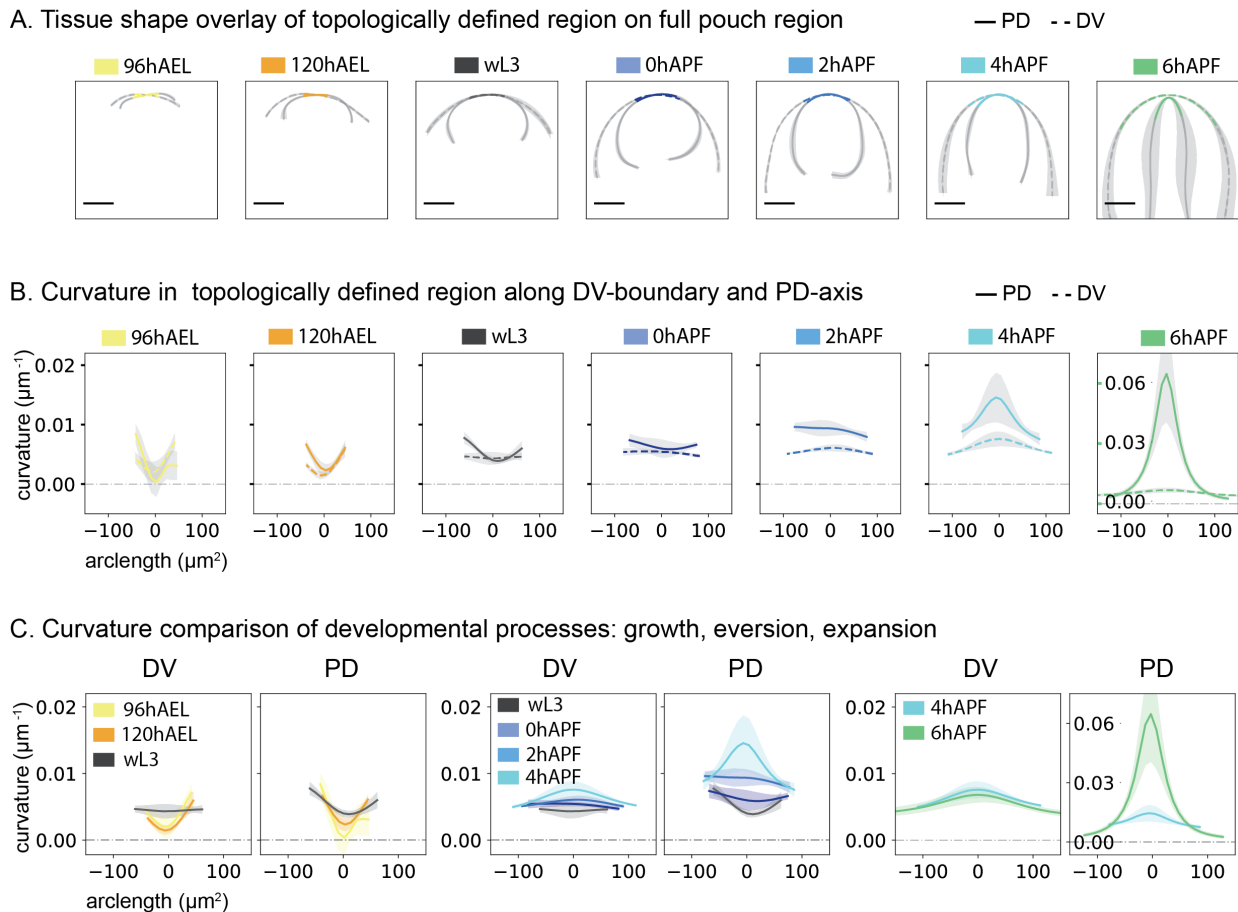


Figure 1-8 | Spatio-temporal analysis of curvature changes by topological region.

Tissue shape overlay of the topologically defined region with the full pouch shape along DV and PD-axis for developmental stages 96hAEL, 120hAEL, wL3, 0,2,4 and 6 hAPF. DV = dashed line, PD = solid line. Mean shape curves for all stages and all discs analyzed along DV- and PD-axis, grey region indicates the 95% confidence interval of the mean for x and y position (A). Curvature quantification in topologically defined region along the apical shape by arclength, grey region indicates the 95% confidence interval of the mean for the curvature, y-axis is indicated on the left for all stages except 6 hAPF, where the y-axis is indicated on the plot (D). Tissue curvature changes for DV and PD-axis, over developmental processes: growth (96hAEL, 120hAEL, wL3), eversion (wL3, 0,2,4 hAPF) and expansion (4 and 6 hAPF). Shaded region 95% confidence interval of the mean in the color of the respective developmental stage. Y-axis are the same between DV and PD for growth and eversion (C). Scalebars = 100μm

### 1.2.5 Topological binning reproduces previous results on larval stages

The topological distance method and the definition of the tissue center constitutes a coarse-grained approach to understand cell packing patterns. Different aspects average out more subtle effects of radial cell packing patterns: Most importantly, the definition of the tissue center is susceptible to a certain amount of noise, and topological bins are, as a consequence of cell shape heterogeneity, not perfectly circular.

To understand the significance of these effects, I tested whether the topological method can recapitulate the published cell packing patterns. To test consistency, I compare 96 hAEL and 120 hAEL timepoints with the published data from Dye, Popović et al., 2021. The published data covers a developmental time from 96 hAEL + 13 hr in culture and throughout this time period, no changes in the pattern of cell morphology has been observed. Thus, if the topological method is able to reproduce previous results, the values for the 96 hAEL timepoint should correspond to those published. Moreover the 120 hAEL should add more information on the changes between day four and five of development.

I do not observe changes in the cell area profile between 96 and 120 hAEL, using the topological method (Figure 1-9 A). To compare this data to the published results, the metric distance to the topologically defined tissue center for each cell is calculated. This confirms that the new data is in accordance with the previously published area profile in both regions and timepoints (Figure 1-9 A, B). Dye, Popović et al., report also a radial gradient of tangential cell elongation based on radial projection  $Q_{rr}$  of the cell elongation tensor. I observe a similar elongation profile for 96 hAEL, but at 120 hAEL the gradient of tangential cell elongation decreases, revealing temporal changes in the cell elongation pattern. This, gradual decrease in cell elongation towards the end of larval growth has been previously observed (Mao et al., 2013) (Figure 1-9 C). Applying the same comparison to the DV-boundary, I find that the elongation profile along the DV-boundary ( $Q_{xx}$ ) is in accordance with previous results: Cells are elongated along the direction of the DV-boundary without a spatial gradient (Figure 1-9 D).

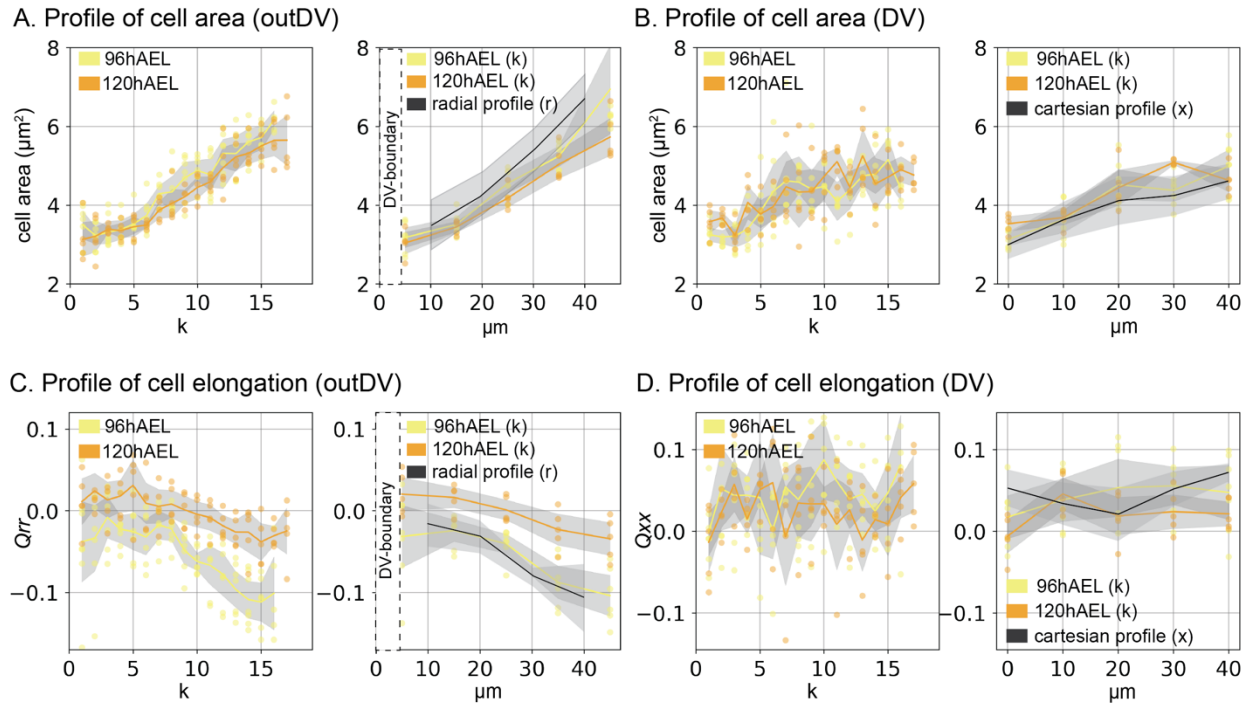


Figure 1-9 | Topological binning method reproduces previous results

Datapoints show the mean values per disc and for each spatial distance for cell area (A,B, outDV and DV regions) and the radial component of cell elongation ( $Q_{rr}$ ) (outDV, C) and the  $xx$  component of cell elongation ( $Q_{xx}$ ) (DV, D) For spatial plots in metric distance ( $\mu\text{m}$ ) we use a similar coarse graining to the one previously published, with the exception, that for the outDV region, we exclude only the DV-boundary and not a  $10\mu\text{m}$  wide region around the DV-boundary as done previously. We round to nearest intervals of  $10\mu\text{m}$  and display the average value for each disc analyzed. Colors represent developmental stages; lines present the average from all datapoints. The grey region around the 96 and 120 hAEL stages shows the 95% confidence interval of the mean. Radial and cartesian profiles are taken from Dye, Popović et al., 2021. For this dataset the shaded region shows the standard deviation.

### 1.2.6 Summary topological method for spatial analysis

Overall, the new method presented here can recapitulate previously described patterns in packing geometry, and can approximate radial and cartesian coordinates by topology. The topological binning method is applicable for any tissue geometry and allows for different parameters depending on the tissue geometry and morphological landmarks. We also establish a methodology to map spatial changes over different developmental timepoints based on  $K_{ref}$  without the need for live imaging and cell tracking. I have further identified the tissue shape changes that are happening in the topologically defined region, providing the toolset to address cellular contributions to tissue shape changes during wing disc evagination.

## 1.3 Cell packing geometry during evagination

### 1.3.1 Cell shape variability decreases over evagination

To understand how the tissue shape changes are accomplished I investigate the changes in cellular packing geometry at the apical surface, starting with cell area (Figure 1-10). The tissue wide average of cell areas increases by ~3-fold during eversion and expansion. During the growth phases cell areas do not increase dramatically, although cells in the DV-boundary are initially smaller than the outDV cells, this difference vanishes at 120hAEL. There are no significant differences between the DV and outDV regions at most stages, except for 96 hAEL. Yet, cell area increase follows different kinetics between different regions during eversion. From 0 to 2 hAPF cell areas increase in the outDV region, but not in the DV boundary, while the opposite is the case from 2 to 4 hAPF. At 4 and 6hAPF, disc-to-disc variability for average cell areas increases. This result could merge from the more dramatic change in area that occurs during this time period, where the wing pouch doubles its apical surface area within 2 hr of development. Importantly, any small variations in developmental staging could have a high impact if changes are rapid in time. This variability in staging was also seen different progress in PE removal that I observe at 4 hAPF (Figure 1-10 A,B).

I investigated whether the area variability between discs is mimicked in the area variability within the disc. To test this idea, I calculate the coefficient of variation for cell area in each disc as a measure for inter-tissue variability of cell shapes:

$$CV = \frac{\sigma}{\mu} \text{ with } \mu = \frac{\sum a}{N} \text{ and } \sigma = \sqrt{\frac{\sum (ai - \mu)^2}{N}}$$

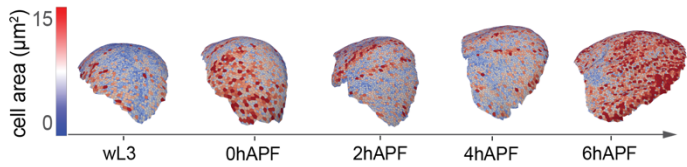
Where  $a$  is the cell area, and  $N$  the number of cells. I find that the  $CV$  decreases over growth and eversion outside the DV-boundary and increases slightly at expansion. The  $CV$  in the DV-boundary drops at puparium formation and remains constant thereafter (Figure 1-10 C).

Another property tightly linked with cell area and growth is the number of neighbors per cell. Larger cells tend to have more neighbors, and cell divisions and rearrangements change the polygon distribution locally. Accordingly, fractions for different polygons can be used as a readout for developmental processes and mechanical state of the tissue. In accordance with previous

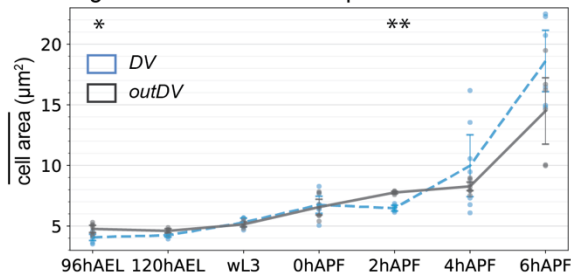
reports for growing epithelia, the fraction of cells with n neighbors ( $P_n$ ) is highest for hexagons at larval stages (Farhadifar et al., 2007). During late larval growth the fraction of hexagons increases slightly, while 4,7 and 8-sided cells decrease, this is in accordance with the growth rates slowing down at the end of larval development (Figure 1-10 D-F). During evagination, the fraction of hexagons increases even further up to 50% of all cells in the tissue, while 5,4 and 8-sided polygons decrease and the number of heptagons remains stable (Figure 1-10 F). This increase in hexagons could be attributed to the lack of dividing cells, the increase in cell areas, or a tissue state transition towards fewer rearrangements and a predominantly elastic behavior.

My data is however in slight disagreement with reports from 96 hAEL and 120 hAEL timepoints, that observe a similar increase in hexagons, yet the fraction of hexagons is even higher for these timepoints as compared to the fraction observed here (Sánchez-Gutiérrez et al., 2013). Potential reasons for this could be variability in developmental timing, or a methodological difference by the cutoff length at which bonds are considered vertices.

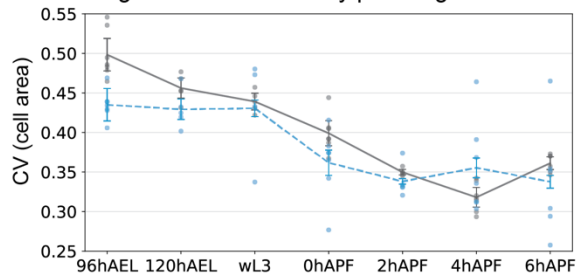
### A. Cell area distribution examples



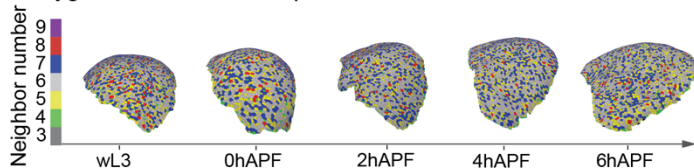
### B. Average cell area over development



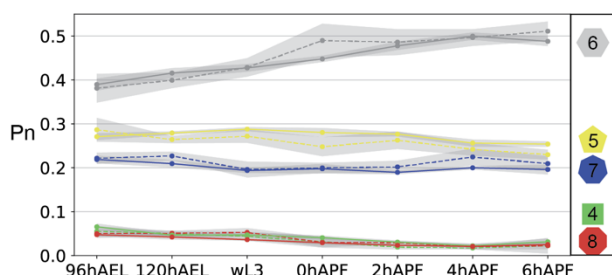
### C. Average cell area variability per wing disc



### D. Polygon distribution examples



### E. Fraction of polygons (Pn) over time



### F. Change in Pn over evagination

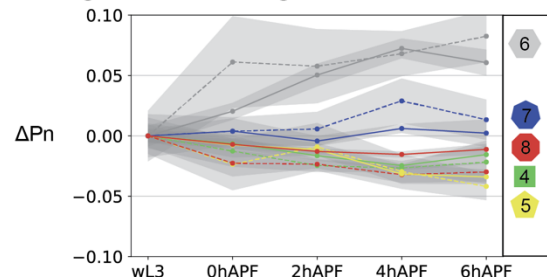


Figure 1-10 | Cell area and packing topology distributions over evagination

Exemplary images of cell area and polygon distribution in the segmented region, showing the full pouch for wL3 and dorsal side for pupal stages (A, D). Average cell area and average CV of cell area in the topologically tracked region, black = outDV, blue = DV-boundary. Datapoints show averages for discs, line shows the average over all discs, error bars show the 95% confidence interval of the mean (B, C). Fraction of Polygons (Pn) in the topologically tracked region. Fractions for polygon classes over development (E) and change in fraction ( $\Delta Pn$ ) as compared to wL3 (F). Colors indicate polygon class, dashed line = DV-boundary, solid line = outDV. Asterisks show statistical significance for the difference in average area between DV and outDV (Mann-Whitney U, two-sided, method=exact, \*\*:  $1.00e-03 < p \leq 1.00e-02$ , \*:  $1.00e-02 < p \leq 5.00e-02$ . No asterisk:  $5.00e-02 < p$ )

### 1.3.2 Spatial patterns of cell area increase during eversion

As seen in the previous chapter, cell areas increase during eversion and the same time the cell packing geometry becomes more ordered, as the CV of cell area decreases and the fraction of hexagons increase. One mechanism by which these phenomena could be coupled is a differential cell area increase, leading to a more homogenous area pattern throughout the tissue.

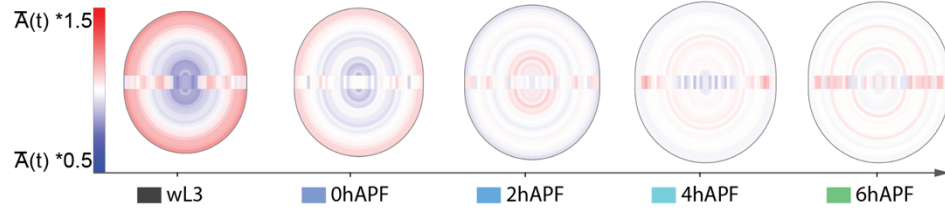
Given the previously identified radial organization in the wing pouch, and the relatively simple geometrical implication of polar coordinates radially organized cell behaviors are also a possible candidate for driving morphogenesis. To test, whether radial patterns in cell packing geometry change together with tissue shape changes, I use  $K_{ref}$  as a spatial metric, allowing for direct comparison of cell shape properties between timepoints by topological position (for reference Figure 1-7 C).

At wL3 stage, the cell area profile resembles the area profile at larval growth stages, cells in the center are smaller than the periphery. However, the gradient is shallower, with a 1.5-fold area increase from center to out over the segmented region, as compared to a 2-fold increase at growth stages. Interestingly, during eversion, this pattern of cell size vanished and cell size becomes homogenous along  $K_{ref}$ . This homogenous area distribution is maintained at wing expansion, although cell areas further increase (Figure 1-11 A, B). In the DV-boundary, cell areas at wL3 stage are small in the first 5 bins from the center of the wing disc and larger thereafter. This anisotropy in cell area distribution vanishes at 0 hAPF and subsequently cell areas are homogenously distributed along the DV-boundary (Figure 1-11 A, D).

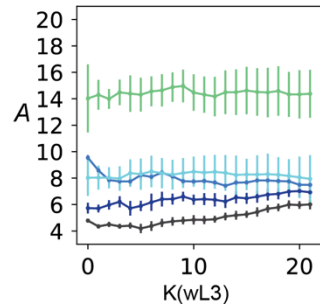
Thus far I have compared cell area gradients using the wL3 stage as reference timepoint for  $K_{ref}$ . Yet, the temporal dynamics of cell area increase are inhomogeneous. To address how this area increase is achieved sequentially, I compare the spatial changes in cell area ( $A(\text{final})/A(\text{reference})$ ) over  $K_{ref}$  for consecutive timepoints (Figure 1-11 C, E). This analysis reveals that, in the outDV region, at the transition from larva to pupa (wL3 to 0 hAPF), cell areas increase by a factor of 1.5 in the center of the disc, and less in the periphery. This in-homogenous increase is also observed for the transition between 0- 2 hAPF. All subsequent changes are homogenous, yet from 2- 4 hAPF, cell areas increase only a little, while at the next timestep from 4- 6 hAPF, cells nearly double their areas (Figure 1-11 C). Interestingly, the temporal dynamics are different

in the DV-boundary: Cells in the DV-boundary increase from wL3 to 0 hAPF and after 2 hAPF (Figure 1-11 E). Accordingly, there is a quiescent or reduced phase for cell area expansion at 2- 4 hAPF outside the DV-boundary and at 0- 2 hAPF inside the DV-boundary.

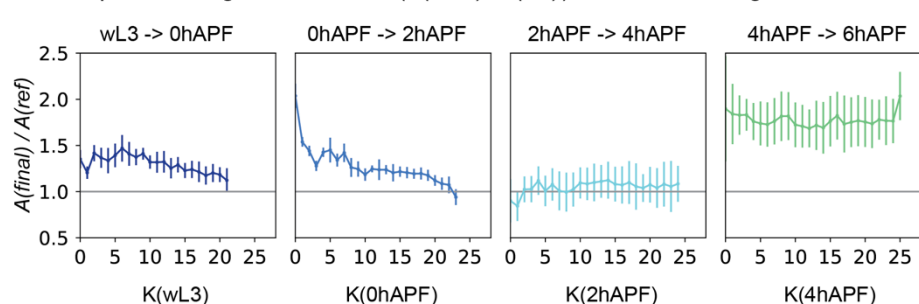
A. Geometric visualization of the cell area profile ( $A(k)$ )



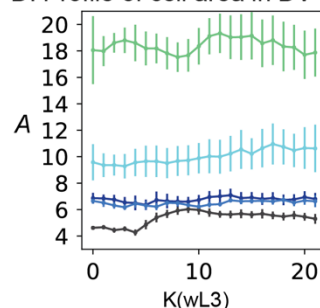
B. Profile of cell area in outDV



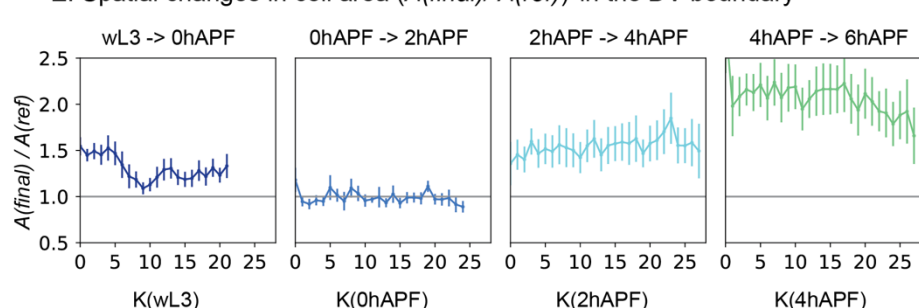
C. Spatial changes in cell area ( $A(\text{final})/A(\text{ref})$ ) in the outDV region



D. Profile of cell area in DV



E. Spatial changes in cell area ( $A(\text{final})/A(\text{ref})$ ) in the DV-boundary



F. Geometric visualization of spatial changes in cell area ( $A(\text{final})/A(\text{ref})$ )

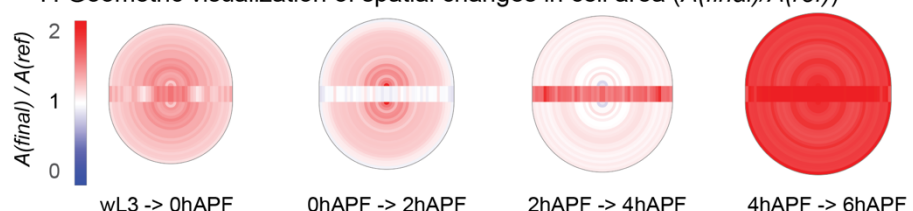


Figure 1-11 | Changes in cell area profile during evagination

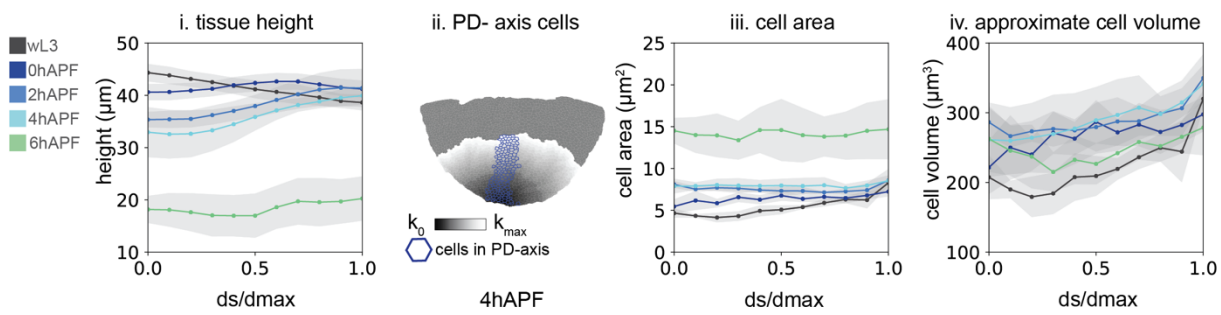
Geometric visualization of the wing pouch over different stages. Each topological bin is colored by its average property from all discs analyzed. Spatial binning in the outDV region is visualized as half-circles; spatial bins of the DV-boundary are visualized by a rectangular box, separating the two sides of the outDV region (A, F). Geometric visualization of cell area distribution. Color code is calculated for each timepoint by the average cell area per timepoint +/- half the average area. Profile of cell area over  $K$ , where  $k(wL3)$  is used as reference, for outDV (B) and DV-boundary region (D). Colors correspond to developmental stages as indicated in A. Spatial profile of consecutive cell area changes ( $A(\text{final})/A(\text{ref})$ ). Timesteps for each plot are indicated above; colors correspond to the respective final timepoint;  $K$  is based on  $k(\text{initial})$  (C, E). Changes in area for outDV (C) and DV-boundary (E). Geometric visualization of spatial area changes. Color code corresponds to  $A(\text{final})/A(\text{ref})$ . Values <1 indicate a decrease in cell area (blue), values >1 indicate area increase (red). Geometric visualization is based on  $K_{\text{ref}}$ . Consecutive timesteps are indicated below (F)

### **1.3.3 Tissue growth during eversion and expansion**

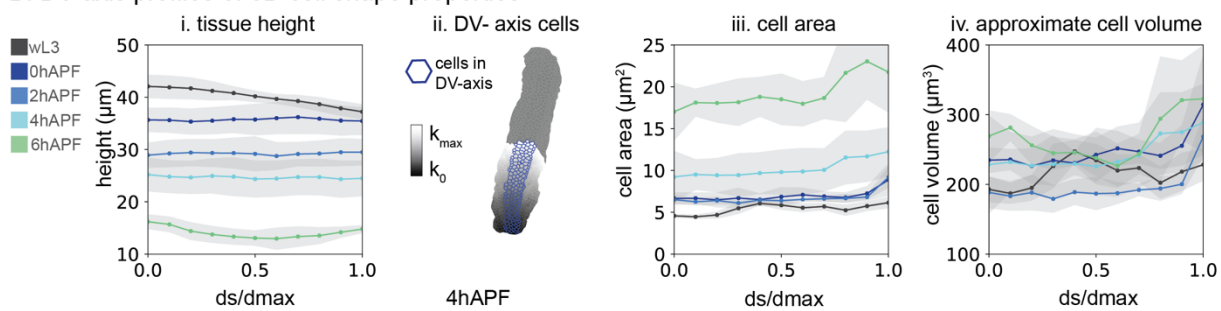
To test if the observed area increases are due to a 3D cell shape change or due to cell volume growth, I tested whether they are anticorrelated with the observed height changes and if cell volumes are conserved. I use the height profiles along DV and PD-directions and limit the analysis to the max distance ( $d_{max}$ ) observed for each developmental stage based on  $K_{ref}$  (Figure 1-12 A.i, B.i). Cells in pseudostratified epithelia experience changes in their cross-sectional area along their apico-basal direction. Yet, these effects average out over tissue patches, when a similar packing density is given along the apico-basal direction. Thus, to estimate cell volume one can assume a cylindrical shape, with the cross-sectional area given by the apical cell area and  $V = A * h$  where  $V$  is the Volume,  $A$  is the apical cell area in  $\mu\text{m}^2$  and  $h$  is the tissue height approximation, given by the smallest distance between the apical and basal DP surfaces. To estimate cell volumes along the PD-direction, I use a stripe of cells in the tissue center that contains six cells for each topological distance. The cells are defined by the maximum topological distance to the cell next to the DV-boundary ( $k(DV)$ ) at maximum  $k$  (so called  $k$  (Edge) see materials and methods). To estimate cell volumes along the DV-direction, I use all cells of the DV-boundary up to a length of maximum  $k$ , as the DV-boundary is only a few cells wide and the height analysis does not pick up changes along the DV-width (Figure 1-12 A., B).

We observe that cell volumes increase slightly along the PD-direction at 2 and 4 hAPF and decrease again at 6 hAPF, but the slope does not change over development ( $p$  values  $> 0.05$  for all stages as compared to wL3). Along the DV-boundary, we do not observe significant changes in cell volume, except for a small increase at 6 hAPF ( $p = 0.017$ ) and we do not observe changes spatial changes along the DV-boundary (Figure 1-12 C). These data indicate that cell area expansion and height decrease are anticorrelated during eversion and no differential volume increase is observed, although small, transient changes in cell volume might occur.

### A. PD-axis profiles of 3D cell shape properties



### B. DV-axis profiles of 3D cell shape properties



### C. Average cell volume and slope over development

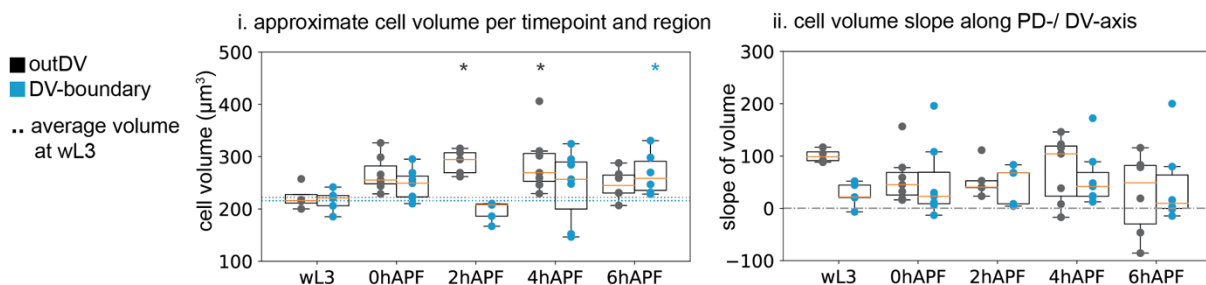


Figure 1-12 | Tissue height and cell volume changes during evagination

Spatial profiles by a fraction of distance over the maximum distance covered (ds/dmax). ds/dmax is averaged in 0.1 steps, developmental stages are indicated by color, grey region shows 95% confidence of the mean for all wing discs analyzed. One exemplary image of a 4 hAPF wing disc for each direction is shown, outlined are the cells for the respective direction in blue, and  $k$  is indicated as greyscale (A.ii., B.ii.). Tissue height (i), cell area (iii) and approximate cell volume (iv) are calculated along the PD-axis (A) and the DV-boundary (B). Average cell volume (C.i.) and slope (C.ii.), for outDV in black and DV-boundary in blue. Each datapoint is one wing disc, boxplots show the median in orange, box shows upper and lower quartile values, whiskers extend 1.5 beyond upper and lower quartile. Dotted line shows the mean for wL3, for each region calculated individually. Dashed line indicates zero slope for comparison (C). Asterisks show statistical significance for each timepoint as compared to wL3 of the same region (Mann-Whitney U, two-sided, method=exact, \*:  $1.00\text{e-}02 < p \leq 5.00\text{e-}02$ . No asterisk:  $5.00\text{e-}02 < p$ )

### 1.3.4 The magnitude of cell elongation does not change during eversion

As previously observed and confirmed by my analysis cells are elongated tangentially in the growing wing disc at 96 hAEL (see section 1.2.5). But the orientation and magnitude of cell elongation changes towards the end of larval growth (Dye et al., 2017; Mao et al., 2013). Cell elongations can have different implications for tissue geometry and morphogenesis: The magnitude of cell elongation, is a measure for cell shape anisotropy and can indicate mechanical state changes in the tissue (Atia et al., 2018). I observe that towards the end of wing disc growth, the magnitude of cell elongations decreases in DV-boundary and outDV regions. The magnitude of cell elongation does, however not change during subsequent evagination in the outDV region and only transiently increases in the DV-boundary at 0 and 2 hAPF (Figure 1-13 A). The spatial pattern of cell elongation does not change in the outDV region during evagination.

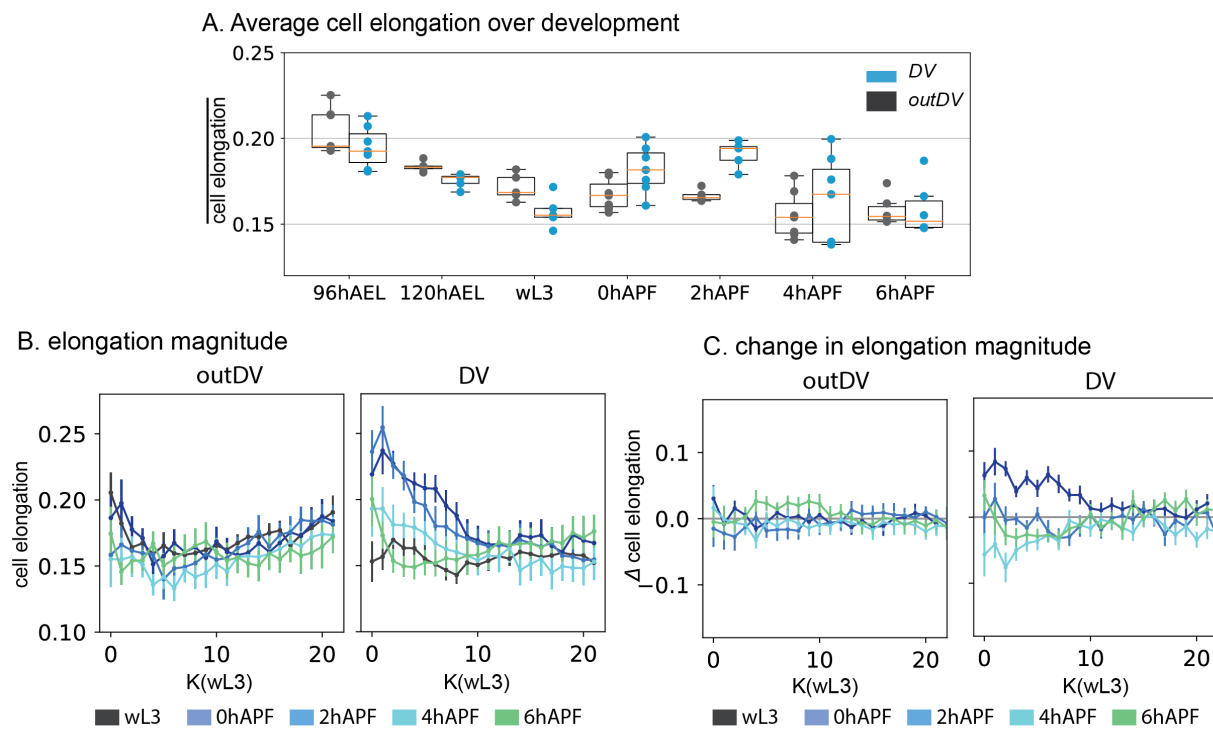


Figure 1-13 | The magnitude of cell elongation decreases at the end of the growth phase

Average cell elongation magnitude for all disc of a developmental timepoint, each datapoint is the average from one wing disc, boxplots show the median in orange, box shows upper and lower quartile values, whiskers extend 1.5 beyond upper and lower quartile (A). Spatial plots of cell elongation (B) and change in cell elongation ( $\Delta$  cell elongation) (C) over  $K(wL3)$ . outDV and DV-boundary are plotted separately; colors correspond to developmental stages (B, C)

This is different in the DV-boundary, here, during early eversion, cells are transiently more elongated at small  $k$  (Figure 1-13 B). Correspondingly, anisotropic changes in elongation magnitude are observed in at these stages (Figure 1-13 C).

### 1.3.5 Changes in global cell elongation nematic rule out cell elongation as driving force for evagination

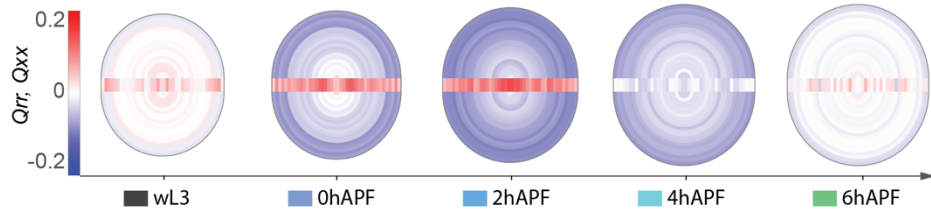
Contributions to morphogenesis from cell elongation depend on the orientation of cell elongations. Yet, the magnitude of cell elongation does not contain information on the directionality of the elongated cell. Cellular packing geometry in the wing disc is characterized by a pattern of tangentially elongated cells. A similar elongation pattern has been observed in the leg imaginal disc, and it has been proposed that such a pre-pattern of packing geometry could be resolved to facilitate tissue morphogenesis during leg evagination (Condic et al., 1991). This provides an attractive hypothesis given the more recent observations, that at late growth stages in the wing disc, the cell elongation pattern could be actively generated by rearrangements (Dye et al., 2021). Thus, a prepattern mechanism could provide an explanation for this behavior. To test if this is true, I tested the radial projection  $Q_{rr}$  and the component of elongation along the DV-boundary ( $Q_{xx}$ ) of the cell elongation tensor at wL3 to 6 hAPF (Dye et al., 2021). My analysis of 120 hAEL already revealed a shallower gradient and on average slightly radial elongation in the center and more tangential elongation in the periphery, as compared to 96 hAEL (Figure 1-9 C). This tendency towards a more undirected cell elongation is continued to wL3 stage, where we observe no gradient and no tissue wide orientation of cell elongations in radial or tangential direction ( $Q_{rr} \approx 0$ ) (Figure 1-14 A, B). This observation rules out a possible contribution of an elongation prepattern in the outDV region for eversion. Over eversion (0-4 hAPF) cells become again elongated tangentially to the center, starting from  $Q_{rr} \approx 0$  in the center to a maximum tangential elongation of  $Q_{rr} \approx -0.07$  in the periphery. At tissue expansion (6 hAPF) this gradient of cell elongation has resolved and no orientation of cell elongations are detectable ( $Q_{rr} \approx 0$ ) (Figure 1-14 A, B). The relative changes in elongation reveals that the most dramatic and in-homogenous change towards tangential elongations outside the DV-boundary occurs at the transition from wL3 to 0 hAPF. Between 0 to 2 hAPF and 2 to 4 hAPF changes in elongation

are uniform, first increasing tangentially then decreasing slightly to become more radial. This trend is continued from 4 to 6 hAPF, with a slightly larger effect in the periphery, regenerating the already described ‘neutral’ elongation profile (Figure 1-14 C, F).

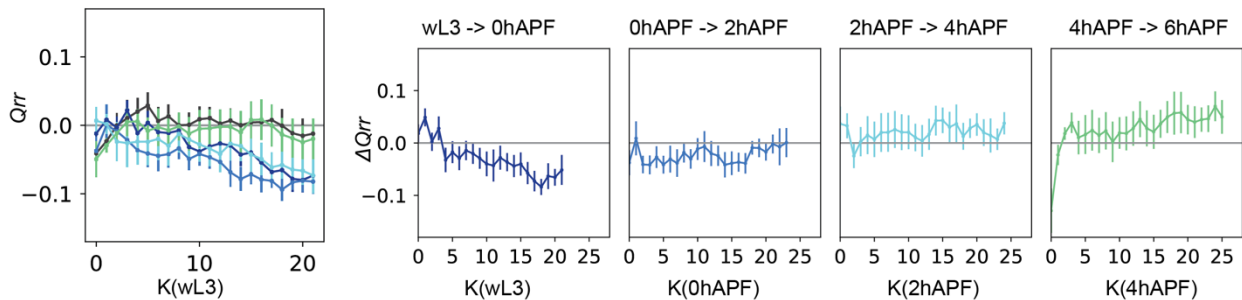
The orientation of cell elongation in the DV-boundary at wL3 stage is similar to the growth stages and cells continue to be elongated towards the center ( $Q_{xx} \approx 0.05$ ) (Figure 1-14 A, D). Cell elongations are even more elongated towards the center at 0 and 2 hAPF, and become slightly more tangential at 4hAPF ( $\Delta Q_{xx} \approx -0.1$ ) and more radial again at expansion (4 to 6 hAPF). (Figure 1-14 D). Accordingly, the direction of the change in the orientation of cell elongations ( $\Delta Q_{xx}$ ) changes from initially radial, to tangential at 4 hAPF and radial again at 6 hAPF (Figure 1-14 E, F).

Taken together, we observe that the orientation of cell elongation changes multiple times during eversion and expansion. In both regions, the sign of  $\Delta Q_{rr}, \Delta Q_{xx}$ , changes from 2 to 4 hAPF and in the DV-boundary at the transition from eversion to expansion (4 to 6 hAPF). My analysis rules out an elongation driven eversion process as suggested for the wing disc but indicates a dynamic change in cell shapes that may result from tissue level forces or cellular geometry and topology.

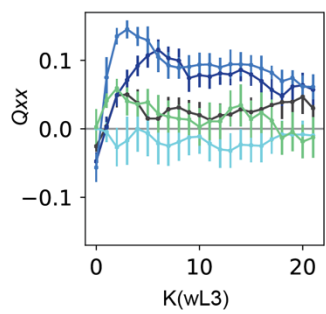
### A. Geometric visualization of the cell elongation profile ( $Q_{rr}$ , $Q_{xx}$ )



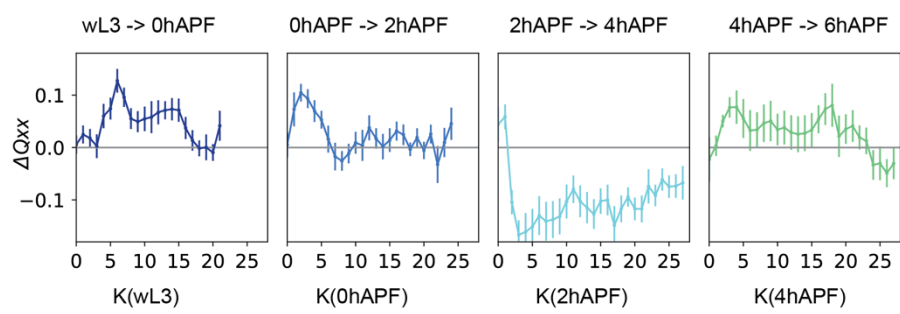
### B. Cell elongation profile (outDV) C. Spatial changes in cell elongation ( $\Delta Q_{rr}$ ) in the outDV region



### D. Cell elongation profile (DV)



### E. Spatial changes in cell elongation ( $\Delta Q_{xx}$ ) in the DV-boundary



### F. Geometric visualization of spatial changes in cell elongation ( $\Delta Q_{rr}$ , $\Delta Q_{xx}$ )

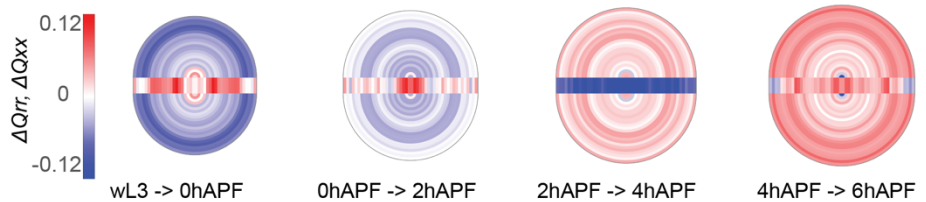


**Figure 1-14 | Changes in cell elongation profile during evagination**

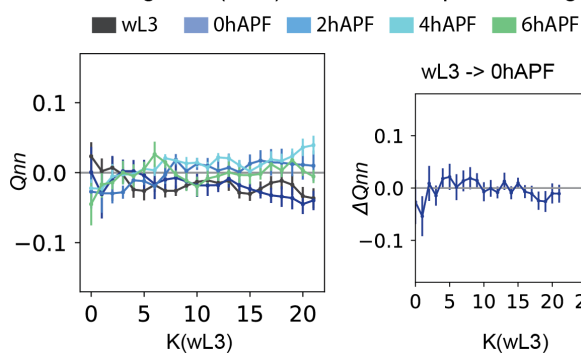
Geometric visualization of the wing pouch over different stages. Each topological bin is colored by its average property from all discs analyzed. Spatial binning in the outDV region is visualized as half-circles, spatial bins of the DV-boundary are visualized by a rectangular box, separating the two sides of the outDV region (A, F). Geometric visualization of cell elongation ( $Q_{rr}$  for outDV,  $Q_{xx}$  for DV). Color code from -0.2 to 0.2: blue values indicate tangential elongation for outDV and orthogonal to the DV for the DV-boundary, red values indicate radial elongation or along DV-boundary, for outDV and DV respectively (A). Profile of  $Q_{rr}/Q_{xx}$  over  $K$ , where  $k$  ( $wL3$ ) is used as reference, for outDV (B) and DV-boundary region (D). Colors correspond to developmental stages as indicated in A. Spatial profile of consecutive cell elongation changes ( $\Delta Q_{rr}$ ,  $\Delta Q_{xx}$ ). Timesteps for each plot are indicated above, colors correspond to the respective final timepoint,  $K$  is based on  $k$  (initial) (C, E). Changes in elongation for outDV (C) and DV-boundary (E). Geometric visualization of spatial elongation changes. Color code corresponds to ( $\Delta Q_{rr}$ ,  $\Delta Q_{xx}$ ). Values greater than zero indicate a change towards more radial, along-DV elongation, values smaller than zero indicate more tangential elongation. Geometric visualization is based on  $K_{ref}$ . Consecutive timesteps are indicated below (F). Error bars indicate the 95% confidence interval of the mean over all disc per timepoint (B-E) t

Analysis of  $Q_{rr}$  and  $Q_{xx}$  assume a specific nematic organization of the tissue, as has been demonstrated in previous literature (Dye et al., 2021). However, I also observe a disagreement in the changes in the magnitude of cell elongation and changes in nematic orientation of cell elongation ( $Q_{rr}$  and  $Q_{xx}$ ). These disagreements can be due to a different nematic organization in the tissue that does not follow a radial, pattern. One potential organizer of tissue nematic properties, for the outDV region, could be the DV-boundary. Thus, I measured the component of cell elongations towards the DV-boundary ( $Q_{nn}$ ) (Figure 1-15 A). Note that at larval stages,  $Q_{nn}$  could be approximated by cartesian coordinates, as the DV-boundary is almost straight. However, during eversion the DV-boundary bends, giving rise to a non-trivial coordinate axis, which depends entirely on tissue geometry. I found that  $Q_{nn}$  does indeed display non-zero values for wL3 and eversion timepoints.  $Q_{nn}$  is slightly negative at wL3 revealing that component of the cell elongation axis aligns with the DV-boundary. At the transition from 2-4hAPF, this pattern reverses and cells elongate more perpendicular to the DV-boundary (Figure 1-15 B, C). However, depending on the shape of the D-boundary, also a negative  $Q_{rr}$  pattern has a component of cell elongation aligning with the DV-boundary. (Figure 1-15 A).

A. Cell elongation ( $Q_{nn}$ ) relative to the DV-boundary



B. Cell elongation ( $Q_{nn}$ )



C. Spatial changes in cell elongation ( $\Delta Q_{nn}$ ) in the outDV region

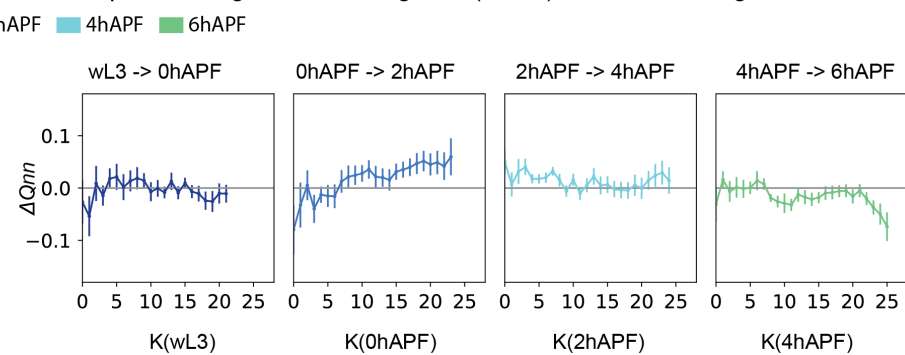


Figure 1-15 | Potential role for the DV-boundary as nematic organizing region

Cartoons showing nematic organization by  $Q_{nn}$  in the outDV region. DV-boundary in orange, outDV region for larval and pupal stages, blue lines indicate the elongation orientation required for negative values of  $Q_{nn}$ , red lines indicate the positive values of  $Q_{nn}$  in the topologically defined region. Profile of  $Q_{nn}$  over  $K$ , where  $k$  (wL3) is used as reference (B) Colors correspond to developmental stages as indicated. Spatial profile of consecutive cell elongation changes ( $\Delta Q_{nn}$ ). Timesteps for each plot are indicated above, colors correspond to the respective final timepoint,  $K$  is based on  $k$  (initial) (C).

Thus, whichever nematic displays larger absolute values can be considered dominant. Since the absolute values for  $Q_{rr}$  are larger than the changes along  $Q_{nn}$ , we conclude that a circular pattern is the dominant pattern during growth and evagination.

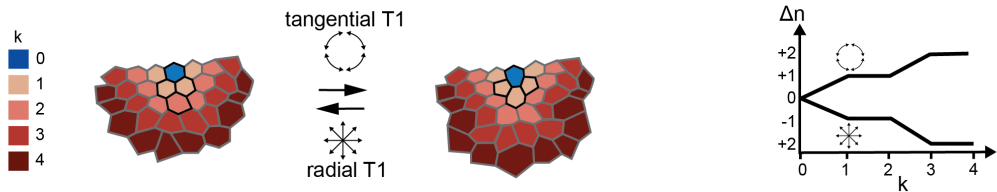
### 1.3.6 Change in tissue topology

The development of tools for the calculation of unidirectional, spatial effects by topological rearrangements was done in collaboration with Abhijeet Krishna

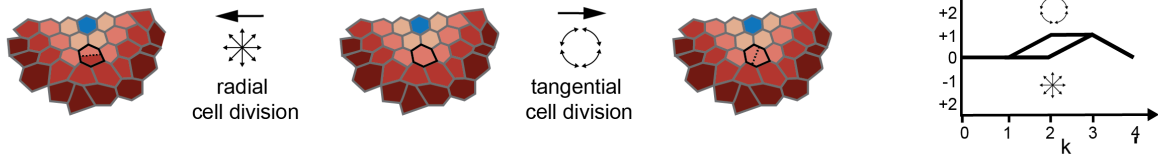
Cell elongation is not the only unidirectional cell behavior that can modulate tissue shape. Oriented cell rearrangements and divisions can also lead to unidirectional effects, thus I decided to further investigate the role of such topological changes in the tissue. Topological changes in the Tissue involve rearrangements, divisions and extrusion and can be quantified on the basis of cell neighbor relationships. T1 transitions can increase or decrease the number of neighbors per cell and thus lead to changes in the topological arrangement of the tissue. Depending on the orientation of the new bond, a T1 transition can be characterized as radial or tangential in orientation. Cell rearrangements by T1 transitions affect not only their immediate neighborhood, but can shift the topological distance for subsequent cells in a complex way that depends on cell shapes and tissue packing topology (Figure 1-16 A.i). This makes it impossible to calculate the absolute number of T1 events, yet collective, unidirectional effects along  $k$  can still be quantified. A similar phenomenological description can be done for cell division and extrusion: Cell divisions always increase the Number of cells per ( $n(k)$ ), yet the daughter cells can either stay in the same  $k$  as the mother or contribute in  $k + 1$ , depending on the orientation of division. A contribution to  $k - 1$  would involve an additional T1 rearrangement and is thus not the immediate effect of the division (Figure 1-16 A.ii). Cell extrusions decrease  $n(k)$  locally (Figure 1-16 A.iii).

A. The number of cells in  $k$  ( $n(k)$ ) depends on topological changes and tissue geometry

A.i.T1 transitions increase or decrease  $n(k)$  and propagate orientation dependent



A.ii.Cell divisions increase  $n(k)$  or  $n(k+1)$  orientation dependent



A.iii.Cell extrusions decrease  $n(k)$

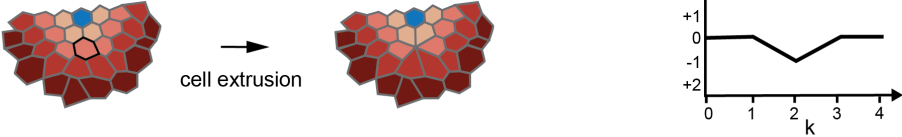


Figure 1-16| The number of cells per  $k$  changes with topology

Different topological changes lead to a change in  $n(k)$ . Graphs show the change in number of cells ( $\Delta n$ ) over  $k$  after a topological change (A). T1 transitions can be tangential or radial, the direction is defined by the orientation of the new bond. T1 transitions affect the number of cells within their topological bin, as well in consecutive bins (A.i) cell divisions increase the number of cells in the topological bin of the mother cell ( $k$ ), or the subsequent bin ( $k+1$ ) (A.ii). Cell death decreases  $n(k)$  for  $k$  of the dying cell (A.iii).

To compare tissue patches over time I preserve the cumulative number of cells ( $N$ ) but allow the maximum  $k$  to change according to topological rearrangements (see section 1.2.3). This relationship between  $N$  and  $k$  contains information about unidirectional topological changes (Figure 1-17 A, C). I observe a non-linear relationship for  $k(N)$  in the outDV-region, and increasing numbers of cells per  $k$  ( $n(k)$ ). Over developmental time,  $k$  needs to increase to achieve the same  $N$ , for the outDV region. This effect is also observable in the decrease in the number of cells for  $k$  ( $n(k)$ ) (Figure 1-17 B). These observations have a number of implications: The topological bins by  $k$  contain more cells as the distance to the center increases. This contributes to the circular shape of the tissue, if  $n(k)$  were constant, one would expect a rectangular shape (under the assumption that cell shapes are uniform along  $k$ ). This is the pattern observed for the DV-boundary. Moreover, I need to include a larger topological distance to the center to contain the same number of cells, as development proceeds, this shows that there is indeed a unidirectional effect

by topological changes. If this weren't the case, any topological changes would average each other out and these tissue wide effects could not be seen. As I need larger  $k$ , it can also be concluded that topological changes happen along  $k$  and not tangential to it. Thus, the cumulative topological changes are oriented along the radial direction.

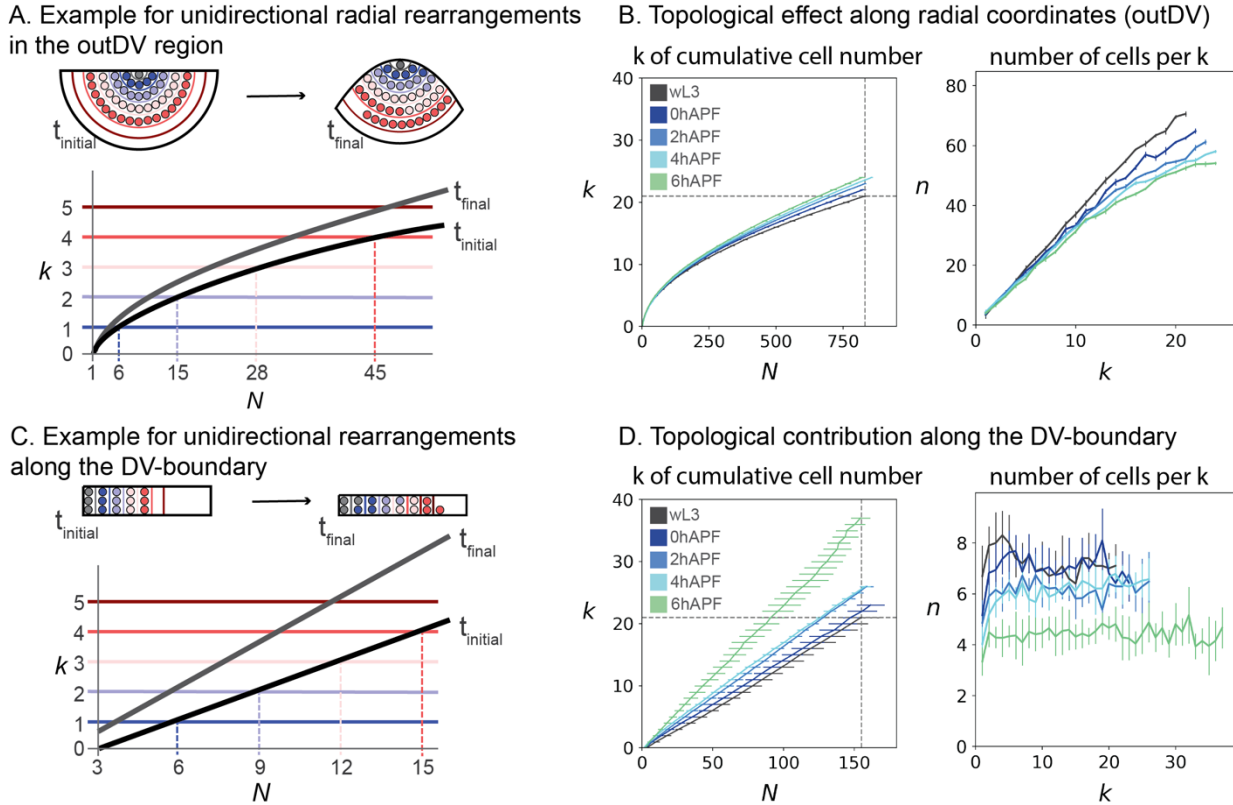


Figure 1-17 | Coarse grained topological effects

The cumulative effects of topological behaviors can be observed by the relationship between  $N$  and  $k$  (A, C). the topological distance  $k$  is plotted against the cumulative number of cells  $N$  and the number of cells per bin ( $n$ ) is plotted against  $k$ . Colors indicate developmental timepoints, error bars show the 95% confidence interval of the mean for the average of all discs per timepoint (B, D). all cells in the topologically defined region of the outDV (B) and DV-boundary (D) regions are quantified. Error bars indicate the 95% confidence interval of the mean over all disc per timepoint (B, D)

This is similar for the DV-boundary, we observe a dramatic increase in  $k$  at maximum  $N$  ( $k(max)$ ):  $k(max) = 21$  to  $k(max) = 27$  after eversion (4 hAPF) and  $k(max) = 38$  at 6 hAPF. For each developmental stage,  $k(N)$  and  $n(k)$  are linear and  $n(k)$  has no slope. This means that the topological width of the DV-boundary does not change by distance to the center and topological changes are uniform.  $N(k)$  decreases over time as compared to the wL3 stage by a factor of 0.8

during eversion, and 0.6 at expansion, similar to the outDV scenario this reveals a unidirectional effect by topological changes along the DV-boundary in xx direction (Figure 1-17D)

Anisotropic contributions to tissue shape cannot directly be compared on  $k$ , as  $k$  changes over time to accommodate the same number of cells.  $k(N)$  shows cumulative effects of topological behaviors, but no spatial information. To understand spatial changes in topology, we further investigate the relationship between  $k$  and  $N$ . For the initial timepoint ( $t$ ), the cumulative number of cells  $N$  is covered by  $k$  distance:  $k(N)$ . The number of cells of a given  $k$  depends on tissue topology and can be defined as  $\Delta_N k(N_i, t)$  where  $i$  is the respective group of cells (topological ring or line for outDV and DV-boundary, respectively) for a given  $k$ . To understand cumulative effects of rearrangements in the DV and outDV region, we can calculate the difference between timepoints ( $t$  and  $\Delta t$ ):

$$\Delta_t k(N_i) = k(N_i, t + \Delta t) - k(N_i, t)$$

From here we get a spatial description of uniaxial contributions for topological rearrangements as:

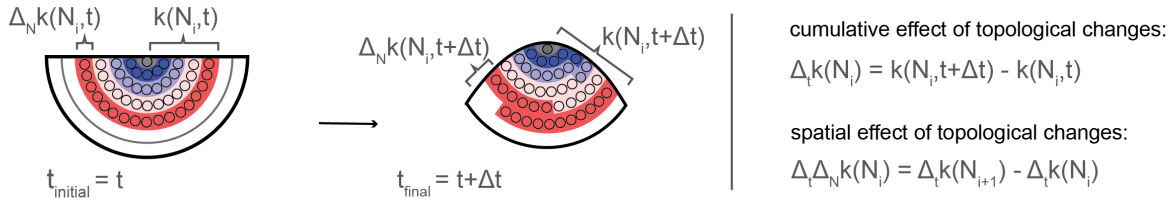
$$\Delta_t \Delta_N k(N_i) = \Delta_t k(N_{i+1}) - \Delta_t k(N_i)$$

We next calculate this value along the direction of  $k$  for the DV and outDV region (Figure 1-18 A). We find, that throughout eversion and expansion,  $\Delta_t \Delta_N k(N_i)$  is positive along  $k$  for the outDV region. This effect leads to an effective tissue expansion along the radial direction, and a shortening along the tangential direction (Figure 1-18 B). In the DV-boundary we observe slightly anisotropic changes in  $\Delta_t \Delta_N k(N_i)$  at wL3 to 0 hAPF and 0-2 hAPF: distally, topological changes elongate the DV-boundary and in the periphery, they lead to a widening. These effects are subtle, however, as compared to the increase in length at 0-2 hAPF and 4-6 hAPF (Figure 1-18 C).

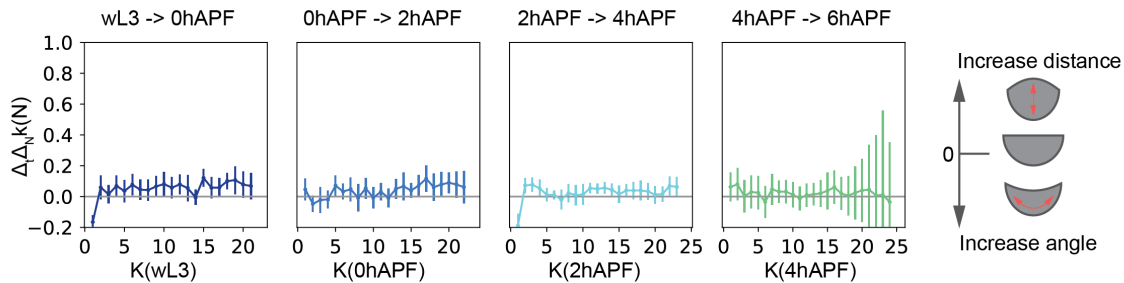
### A. Spatial quantification of unidirectional effects from topological changes $\Delta_t \Delta_N k(N_i)$

$k$  = topological distance coordinates (radial for outDV, along the DV-boundary for DV)

$N$  = cumulative number of cells for topological distance  $k_i$



### B. Topological effect along $k$ in the outDV region



### C. Topological effect along $k$ in the DV-boundary

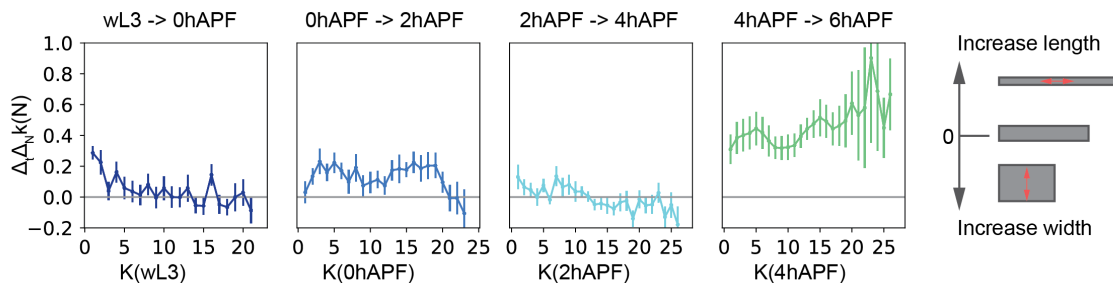


Figure 1-18 | Quantifying unidirectional effects by topological changes

Schematics describing the methodology for spatial topological analysis (A). Spatial contributions by topological changes for consecutive timepoints along  $k$  for outDV and DV-boundary (B, C) Timesteps for each plot are indicated above, colors correspond to the respective final timepoint,  $K$  is based on  $k$  (initial) (B, C). Error bars indicate the 95% confidence interval of the mean over all disc per timepoint (B, C)

Topological changes per  $k$ , change the width of the outDV region and the DV-boundary, yet they are not a measure for the actual topological width, that is, the shortest distance along the width of the DV-boundary. To estimate this effect for the DV-boundary, I compared  $n(k)$  with the topological width of the DV-boundary. I observe, that those two metrics generally agree well with each other. The topological width of the DV-boundary decreases most dramatically at 0-2 hAPF and at 4-6 hAPF as is in accordance with our observations on  $\Delta_t \Delta_N k(N_i)$ . I do observe a mismatch

in the average number of cells per  $k$  and the average number of cells along the DV-width of about 1 cell. This mismatch vanishes at 6 hAPF, indicating that in the case of a few cells along width of the DV-boundary,  $k$  ( $n$ ) leads to an almost perfect approximation of the topological width.

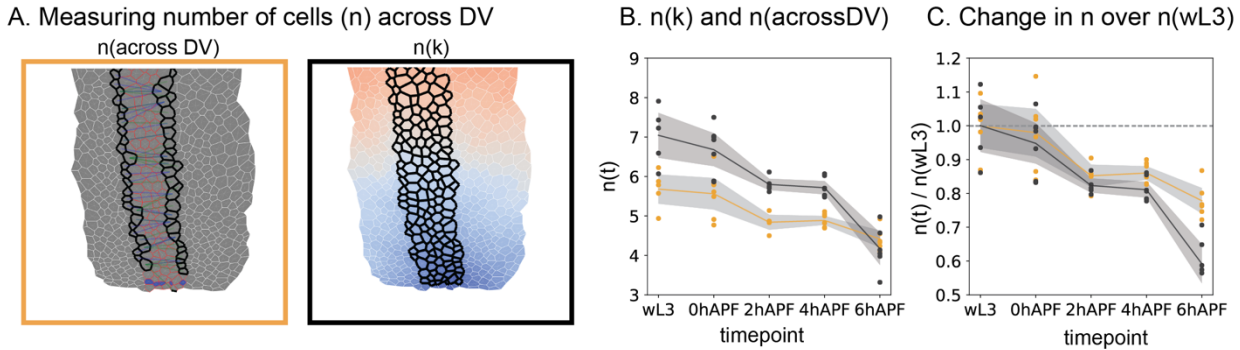


Figure 1-19 |  $n(k)$  resembles the topological width qualitatively, but not quantitatively  
DV-boundary view showing the difference between the shortest topological width ( $n(\text{across DV})$ ) and  $n(k)$  for a 4 hAPF wing disc.  $N(\text{across DV})$  is defined by the topological distance between DV-boundary cells at the margin of the DV-boundary (outlined in black). The DV-boundary cells are outlined in red. For each margin cell the shortest path to the other side is found, blue and green lines indicate such paths. Comparison of average  $n$  for both methods (B) and change in  $n$  over  $n(wl3)$  (C). Each datapoint corresponds to the average for one disc, the grey region shows the 95% confidence interval of the mean (B,C). black =  $n(k)$ , orange =  $(n(\text{across DV}))$

In summary, our methodology can identify cumulative, uniaxial topological effects in static data. Although we are unable to dissect individual contributions by cell division, extrusion and number of rearrangements, we find that topological changes increase the tissue along its proximal-distal direction. This uniaxial effect is likely to contribute to wing disc evagination.

### 1.3.7 Summary wildtype

Our spatial analysis allows us to compare tissue shape changes to spatio-temporal changes in cell packing geometry and topological changes.

From  $wl3$  to  $0hAPF$ : the tissue undergoes only small changes in its curvature along the DV-boundary, but anisotropically increases curvature along the PD-axis. The curvature increases in the center, but not the periphery. During this process, we observe an anisotropic cell area increase in both tissue regions. The uniaxial effect of cell elongations is tangential in the outDV region and along the axis of the DV-boundary, topological effects are both positive, contributing to an increase in length along the radial direction for the outDV region and along the boundary for the DV-boundary

From 0- 2 hAPF: the curvature increases homogeneously along the PD-axis and not along the DV-axis. For cell shapes we observe similar behaviors as between wL3 and 0 hAPF, except that there is no cell area increase in the DV-boundary and the boundary elongation effect by rearrangement becomes stronger at the same time.

From 2- 4 hAPF: tissue curvature increases homogeneously along the PD-axis, and the DV-axis. The area increase is reversed between tissue regions; areas in the DV-boundary increase, whereas they do not change in the outDV region. This area increase is accompanied by a relaxation of cell elongations in the DV-boundary. In the outDV region, elongations and rearrangements are both positive, contributing to radial tissue expansion.

From 4- 6 hAPF: tissue curvature increases further along the PD-axis. I observe homogenous area expansion throughout the tissue and tissue flattening. Cells become isotropic, which contributes to tissue expansion along k and we observe strong uniaxial, positive topological effects along the DV-boundary and continued topological effects along k in the outDV region.

Taken together, I have quantified tissue curvature changes and corresponding cellular size, shape and topology changes throughout all timesteps of evagination. Interestingly, changes in the DV-boundary and outside the DV-boundary can be temporary decoupled, as seen by area changes from 0- 2 and 2- 4 hAPF. Another such decoupling is seen in the changes of cell elongation from wL3 -0 hAPF and 2- 4hAPF. Topological changes appear to be relatively constant in orientation and magnitude over development. They are generally homogenous and positive for the outDV region and positive, yet a bit more variable in the DV-boundary. The only exception is the dramatic increase in rearrangements in the DV-boundary during wing expansion.

Interestingly spatial gradients of cell behaviors are predominantly seen in cell area changes and rearrangements and less in cell elongations. This puts emphasis on an important distinction between cell area changes, and rearrangements and elongation: cell area changes are isotropic deformations and only generate anisotropic tissue shape changes if combined with an inhomogeneous spatial distribution. Rearrangements and cell elongations are always uniaxial and can anisotropic tissue shape changes independently of their spatial distribution.

#### 1.4 Perturbation of cell and tissue shape using MyosinVI RNAi

Our analysis revealed that changes in tissue morphology are accompanied by spatio-temporal changes in cellular packing geometry. To test the effects on changes in cell shape and topological rearrangements, we used a tissue specific knockdown using a UAS-Gal4 approach. We use nubbin-Gal4 (nub-Gal4) to express Gal4 in the wing pouch across all evagination stages. We also observe that Gal4 is expressed over the first fold, surrounding the pouch region (HP-fold) and up to the beginning of the HH-fold on the dorsal side. On the ventral side the expression domain extends covers one additional small fold (Figure 1-20 A).

We decided to knockdown *Drosophila* MyosinVI using a UAS RNAi construct (UAS-MyoVI<sup>RNAi</sup>) construct in the background of Ecad::GFP. MyosinVI is a minus end-directed actin motor protein and has been shown to act as a force sensor by interaction with E-cadherin at adherens junctions. MyosinVI conveys information of junctional tension though its activation of RhoA signaling in response to mechanical stress (Acharya et al., 2018). Apart from that role, it is involved in different cellular processes such as vesicle transport, autophagy, and clathrin-mediated endocytosis (Magistrati & Polo, 2021). It is its potential role as a mechanosensor, that motivated MyosinVI knockdown experiments in the wing disc at 120 hAPF (Dye et al., 2021). In this work, knockdown of MyosinVI leads to a decrease in tangential cell elongation and a flattening of the elongation gradient. At the same time MyosinVI RNAi leads to an increase in cell areas in the wing pouch, while the cell area gradient is not affected. Dye, Popović et al., conclude that the cellular packing geometry and oriented rearrangements in the wing disc arise through a self-organized mechanochemical feedback loop, which can be perturbed by knocking down a mechanosensitive component: MyosinVI. These results motivated us to study the effects of MyosinVI during wing evagination. With MyosinVI RNAi experiments we expect to perturb mechanosensitive cell shape changes as well as topological changes.

#### 1.4.1 MyosinVI knockdown affects tissue shape changes during evagination

We investigated tissue shape changes in the PD-cross-section during evagination in nub-Gal4, MyosinIV knockdown wing discs. It is important to note that only the fold immediately to the pouch (HP-fold) is affected by the knockdown and no major conclusions can be drawn on effects on fold morphology. It can be noticed, however, that the HP-fold does not appear visually different than the HH and HN-folds. Indicating that MyoVI likely has no effect in fold formation or opening during eversion (Figure 1-20 B).

Next, we quantified the shape of the pouch and found, that we do not see any difference along the DV-boundary in  $\text{MyoVI}^{\text{RNAi}}$  as compare to wildtype. Along the PD-axis, the pouch shape at wL3 stage is still similar between  $\text{MyoVI}^{\text{RNAi}}$  and wildtype. Yet, a difference in shape becomes increasingly pronounced as eversion proceeds: In wildtype, the dorsal and ventral half approach each other throughout eversion and expansion, in  $\text{MyoVI}^{\text{RNAi}}$ , the dorsal and ventral half remain remote up to 4 hAPF and approach less than wildtype at 6 hAPF. We also observe that the tissue remains flat, or if anything a bit dented inwards at the DV-boundary during eversion (Figure 1-20 B, C). We further invested tissue shape and curvature in the topologically defined region. We find that at wL3 stage the curvature in both directions resembles the curvature in the wildtype. Unlike the wildtype however, the curvature in the center along the PD-axis decreases and finally reaches zero at the end of eversion, while further away it remains positive. At the expansion (6 hAPF) tissue curvature eventually becomes positive again in the center ( $> 0.01 \mu\text{m}^2$ ). Yet, it is almost 6-fold lower than in the wt. At the DV-axis, as observed by the similarities for tissue shape, we do not observe mayor differences to the wt. However, we saw a minor increase in curvature from wL3 to 4 hAPF in wildtype ( $\sim 0.005 \mu\text{m}^2$ ), which we don't see in  $\text{MyoVI}^{\text{RNAi}}$  (Figure 1-20 D, E). In summary, we observe that MyosinVI knockdown wing discs fail in the apposition of the wing bilayer, and flattening of the dorsal and ventral tissue halves. These changes result in a failure to generate a peak curvature at the future wing margin.

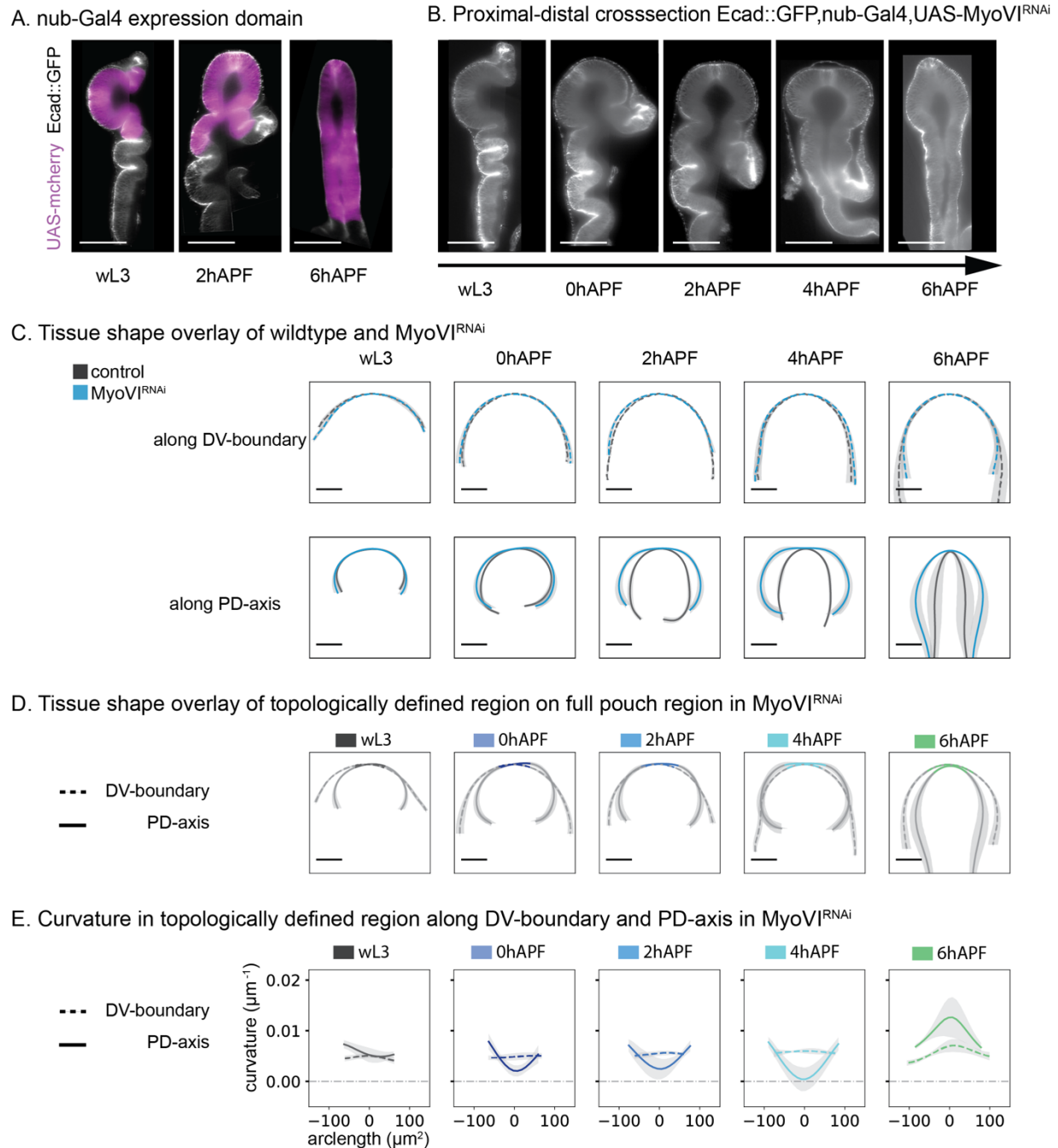


**Figure 1-20 | Tissue shape changes during evagination of MyosinVI knockdown wing discs**

PD-axis crosssection view of wing discs during evagination. Apical cell junctions are labelled with Ecad::GFP (A, B). nub-Gal4 expression domain (magenta) on wL3, 2 hAPF and 6 hAPF (A) nub-Gal4, UAS-MyoVI<sup>RNAi</sup> knockdown discs for developmental stages wL3, 0, 2, 4, 6 hAPF (B). Tissue mean shape overlay between control (Ecad::GFP,nub-Gal4, in black) and MyoVI<sup>RNAi</sup> (blue) wing disc pouch. Along DV-boundary crosssection (dashed line) and along PD-axis (solid line) 95% confidence interval of mean for x and y positions is indicated in grey (C). Tissue shape overlay of full pouch shape and topologically defined region (colors = developmental stage) for MyoVI<sup>RNAi</sup>. DV-boundary = dashed line, along PD-axis = solid line (D). Curvature in  $\mu\text{m}^{-1}$  for MyoVI<sup>RNAi</sup> in topologically defined region. colors = developmental stage, DV-boundary = dashed line, along PD-axis = solid line. Scale bars = 100μm

#### 1.4.2 MyosinVI knockdown affects area increase and cell volume

To test if the shape phenotype can be explained by changes in cell shapes, we next quantified the spatial patterns of cell area and elongation. As expected from the data by Dye et al., 2021, we observe a cell area gradient similar to the gradient in wildtype but with slightly larger cell areas (average cell area: wildtype =  $5\mu\text{m}^2$ , MyoVI<sup>RNAi</sup> =  $7\mu\text{m}^2$  in outDV region at wL3, 95% confidence for slope: wildtype =  $0.080 +/- 0.019$ , MyoVI<sup>RNAi</sup> =  $0.085 +/- 0.023$ ). During tissue morphogenesis, these gradients change: In the outDV region, cell areas expand and the area gradient is resolved by 4 hAPF, whereas cell areas are slightly reduced at 6 hAPF (Figure 1-21 A). In the DV-boundary we do not observe any change in cell areas during eversion, but a more than 2-fold cell area expansion from 4 hAPF to 6 hAPF (Figure 1-21 C).

As compared to the area changes in wildtype, the area increase in the outDV region is qualitatively similar at 4 hAPF, but the spatial dynamics differ: cell areas only start increasing after 0 hAPF. In the DV-boundary, cell areas do not increase during eversion but do so at expansion, this is different from the wildtype, which also expands during tissue expansion but as already obtained a 2-fold area increase by the end of eversion on top of that. The most dramatic change of behavior in MyoVI<sup>RNAi</sup> is observed from 4-6 hAPF in the outDV region, during which cell areas slightly decrease which is contrary to the expansion observed in wildtype (Figure 1-21 B, D).

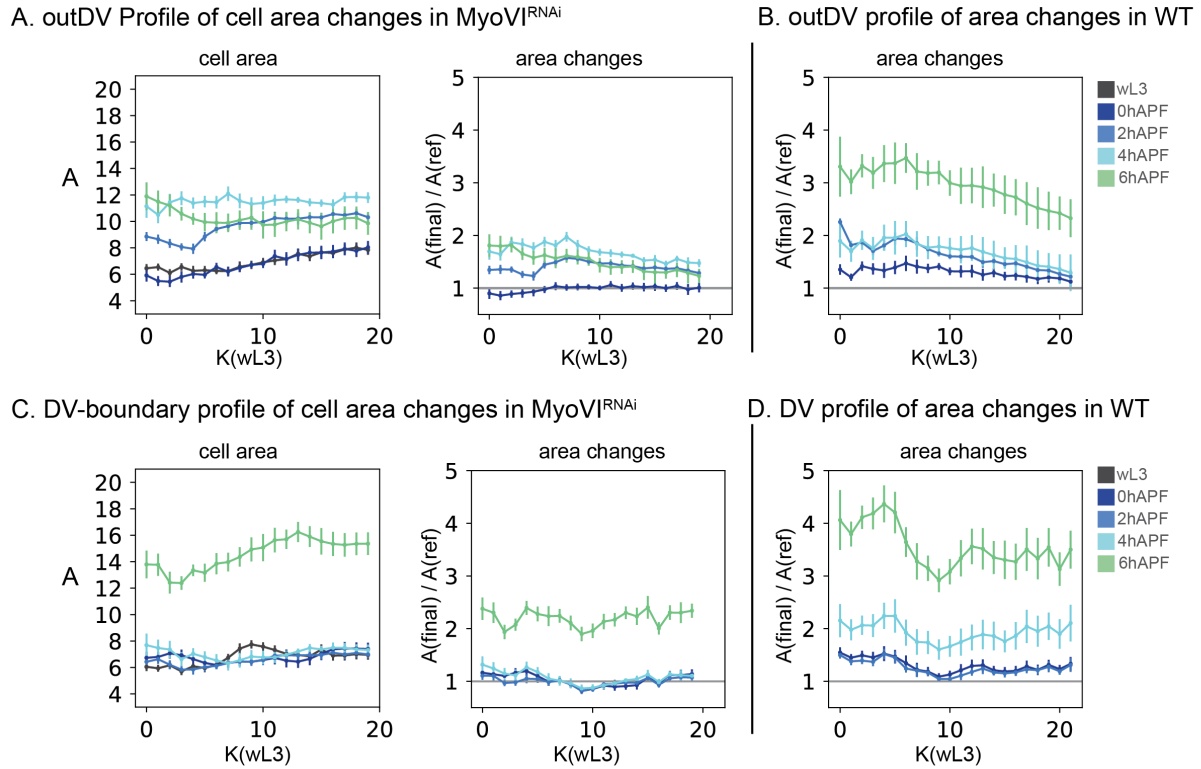


Figure 1-21 | Spatial changes in cell area for  $\text{MyoVI}^{\text{RNAi}}$

Profiles for cell area for  $\text{MyoVI}^{\text{RNAi}}$  (A, C). Profile of cell area over  $K$ , where  $k(\text{wL3})$  is used as reference, for outDV (A) and DV-boundary region (C). Colors correspond to developmental stages as indicated on the right. Spatial profile of consecutive cell area changes ( $A(\text{final})/A(\text{ref})$ ). The reference timepoint is wL3 for all stages, colors correspond to the respective final timepoint,  $K$  is based on  $k(\text{wL3})$  (A, C). Spatial profile of consecutive cell area changes ( $A(\text{final})/A(\text{wL3})$ ) in wildtype for outDV (B) and DV-boundary (D) region. Error bars indicate the 95% confidence interval of the mean over all discs for each timepoint.

To test, if the changes in cell area gradient are due to differential cell volume changes, we quantified tissue height and approximated tissue volume (Figure 1-22 A, C). We observe similar differential changes in cell height as in wildtype, although the pouch fails to flatten as dramatically. Cell volumes are similar to the wildtype for initial stages, yet the slope in volume across the PD-axis is stronger in  $\text{MyoVI}^{\text{RNAi}}$ . We quantify average volume for all timepoints and observe that  $\text{MyoVI}^{\text{RNAi}}$  has a larger cell volume at wL3 as compared to wildtype, which is in accordance with the bigger cell areas at similar tissue height (Figure 1-22 B, D). Next, we tested if there are significant changes in volume over all developmental stages as compared to wL3. In the in the outDV region in wildtype discs, cell volume increases by  $\sim 30\mu\text{m}^3$  (corresponding to an increase by a factor of 1.1-1.2) during eversion and decreases thereafter. In  $\text{MyoVI}^{\text{RNAi}}$  this increase is more dramatic corresponding to a  $\sim 1.7$ -fold increase in cell volume at 4 hAPF (Figure

1-22 B). Interestingly  $\text{MyoVI}^{\text{RNAi}}$  discs temporarily decrease cell volume at the same time in the DV-boundary, while they remain constant in wildtype (Figure 1-22 D).

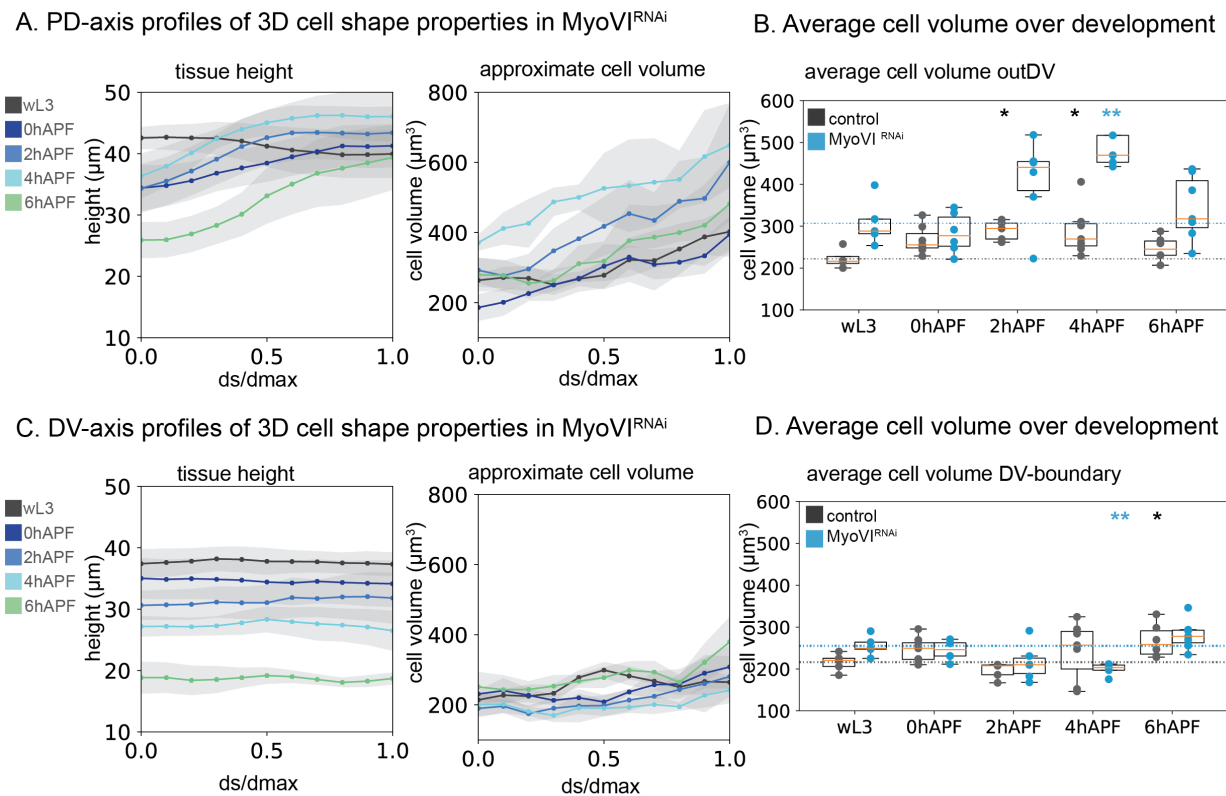


Figure 1-22 | Cell volume changes during  $\text{MyoVI}^{\text{RNAi}}$  evagination

Spatial profiles by a fraction of distance over the maximum distance covered ( $ds/d_{\max}$ ).  $ds/d_{\max}$  is averaged in 0.1 steps, developmental stages are indicated by color, grey region shows 95% confidence of the mean for all wing discs analyzed. Tissue height and approximate cell volume are calculated along the PD-axis (A) and the DV-boundary (C). Average cell volume, for wildtype in black and  $\text{MyoVI}^{\text{RNAi}}$  in blue. Each datapoint is one wing disc, boxplots show the median in orange, box shows upper and lower quartile values, whiskers extend 1.5 beyond upper and lower quartile. Dotted line shows the mean for wL3, for each genotype (B, D). Average volume for the PD-axis (B) and the DV-boundary (D). Asterisks show statistical significance for each timepoint as compared to wL3 of the same genotype (Mann-Whitney U, two-sided, method=exact, \*\*:  $1.00e-03 < p \leq 1.00e-02$ , \*:  $1.00e-02 < p \leq 5.00e-02$ . No asterisk:  $5.00e-02 < p$ )

#### 1.4.3 MyosinVI knockdown affects cell elongation quantitatively but not qualitatively

Dye, Popović et al., reported an effect of MyoVI<sup>RNAi</sup> on cell elongation, this effect might be due to mechanosensitive feedback leading to oriented rearrangements, which in turn can increase cell elongation. But it could also be due to a direct polarizing mechanism leading to cell shape anisotropy. To address effects on, and contributions by, cell elongation, we investigated elongation profiles in MyoVI<sup>RNAi</sup> discs over development. We first compared the elongation profile and average for the outDV region at wL3 stage in wildtype and MyoVI<sup>RNAi</sup> and don't observe significant differences (Figure 1-23 A, C). This result is different from previously published results at 120 hAEL (Dye et al., 2021), indicating that at wL3 stage the initial differences in elongation during wing disc growth have resolved.

Over eversion, cell elongation changes are qualitatively similar between wildtype and MyoVI<sup>RNAi</sup> but quantitative differences are apparent on the average cell elongation: at 0 and 2 hAPF, in the outDV region, cells are more tangentially elongated in wildtype than in the knockdown, and at 4 hAPF cells are elongated more along the DV-boundary in the MyosinVI knockdown as compared to wildtype (Figure 1-23 A, B). The spatial gradients at eversion are similar between wildtype and MyoVI<sup>RNAi</sup>. Cells in the periphery of the outDV region are elongated more tangentially and elongation in the DV-boundary is homogenous (Figure 1-23 C- F). These similar gradients also lead to comparable spatial changes with the exception of the 4 hAPF DV-boundary region, with  $Q_{xx} = 0$  in wildtype and  $Q_{xx} \approx 0.08$  in MyoVI<sup>RNAi</sup> (Figure 1-23 E,F).

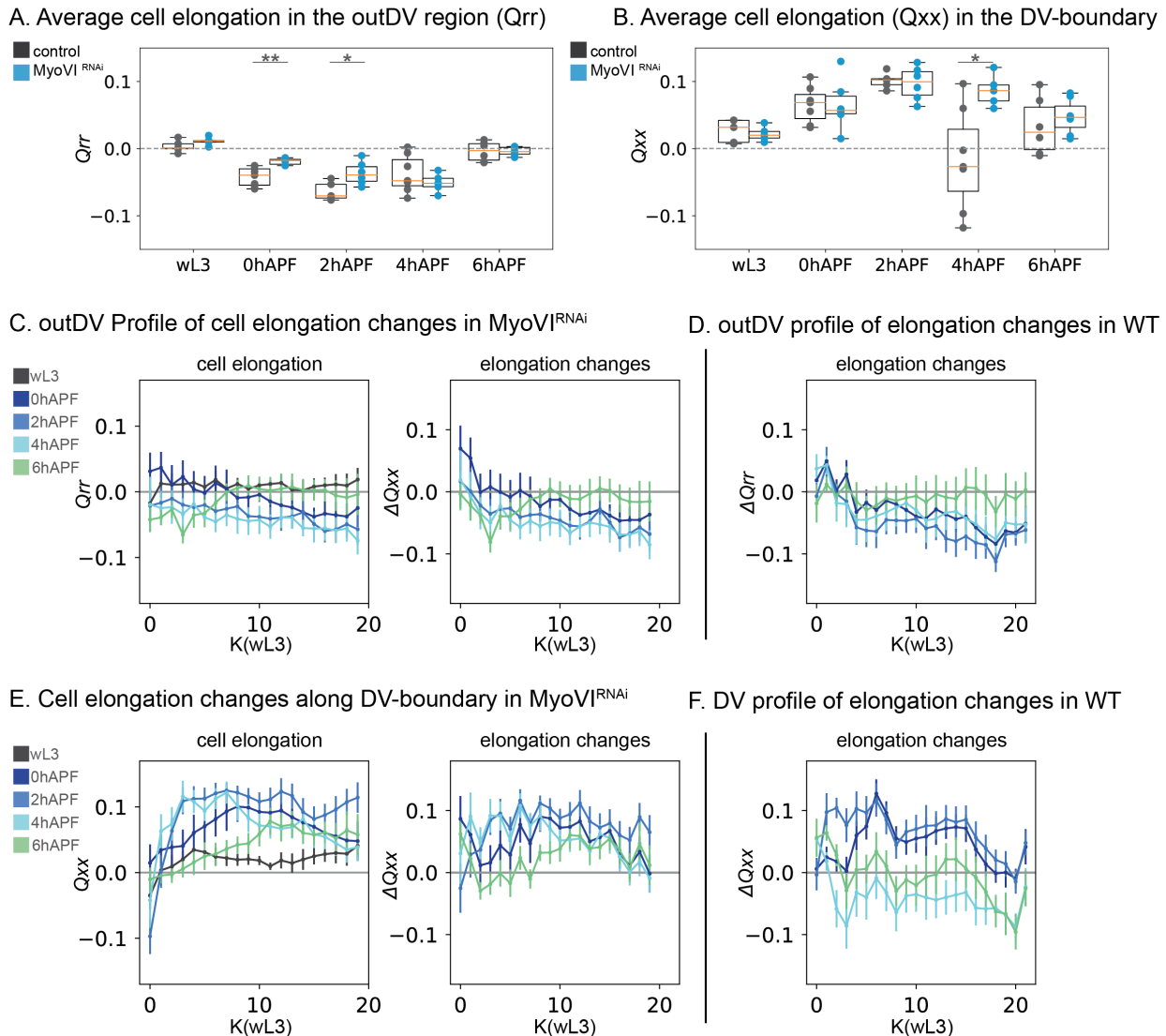


Figure 1-23 | Cell elongation in MyoVI<sup>RNAi</sup>

Average cell elongation: Qrr for outDV (A) and Qxx for the DV-boundary (B). Each datapoint is one wing disc, boxplots show the median in orange, box shows upper and lower quartile values, whiskers extend 1.5 beyond upper and lower quartile. Dashed line shows no cell elongation profile for comparison ( $Q = 0$ ). Average elongation for the outDV region (A) and the DV-boundary (B). Asterisks show statistical significance for each timepoint as compared to wL3 of the same genotype (Mann-Whitney U, two-sided, method=exact, \*\*:  $1.00e-03 < p \leq 1.00e-02$ , \*:  $1.00e-02 < p \leq 5.00e-02$ . No asterisk:  $5.00e-02 < p$  (A, B). Profiles for Qrr (C) and Qxx (E) for MyoVI<sup>RNAi</sup> over K, where  $k(wL3)$  is used as reference, for outDV (C) and DV-boundary region (E). Colors correspond to developmental stages as indicated. Spatial profile of consecutive cell elongation changes  $\Delta Qrr$  (C) and  $\Delta Qxx$  (E). The reference timepoint is wL3 for all stages, colors correspond to the respective final timepoint, K is based on  $k(wL3)$ . Spatial profile of consecutive cell elongation changes  $\Delta Qrr$  (D) and  $\Delta Qxx$  (F) of wildtype discs for comparison. Error bars indicate the 95% confidence interval of the mean over all discs for each timepoint.

#### 1.4.4 Reduced unidirectional topological changes in MyoVI<sup>RNAi</sup>

Given the potential interaction between mechanosensitive signaling via MyosinVI and oriented rearrangements, we next address the topological effects in the tissue. We observe that the maximum topological distance in the outDV region, increases from  $k(\max) = 19$  to for wL3 and 0 hAPF to  $k(\max) = 20$  for 0-6 hAPF (Figure 1-24 A, C).

For the outDV region, spatial analysis reveals an increase in  $\Delta_t \Delta_N k(N_i)$ . This increase is homogenous throughout the tissue, but less than what we observed for the wildtype. As expected by the increase in  $k(\max)$ , we observe  $\Delta_t \Delta_N k(N_i) > 0$  for all timepoints in the outDV region, starting at 2 hAPF. However, we not observe as much of an increase in  $\Delta_t \Delta_N k(N_i)$  over evagination as compared to the wildtype where it continuously increases up to  $\Delta_t \Delta_N k(N_i) > 0.1$  at 6 hAPF (Figure 1-24 A, B, F).

In the DV-boundary we see a increase in the number of cells per  $k$ , which temporarily decreases  $k(\max)$ . This is reflected in the spatial profiles for  $\Delta_t \Delta_N k(N_i)$ , where we first see negative values, which indicates an increase in topological width, followed by a decrease in width at 4 and 6 hAPF. At 4 and 6 hAPF  $\Delta_t \Delta_N k(N_i) \approx 0$  indicating that there is no net effect of topological changes at the end of eversion and expansion. We do not observe a spatial gradient in  $\Delta_t \Delta_N k(N_i)$ , although topological changes appear more spatially heterogenous, which can be an artifact of the small  $n(k)$  (Figure 1-24 C, D, G). The observed behavior in the DV-boundary is different from the wildtype, where topological changes lead to an increase in DV-boundary length most dramatically at 2 hAPF ( $\Delta_t \Delta_N k(N_i) \approx 0.2$ ) and at 6 hAPF where  $\Delta_t \Delta_N k(N_i) \approx 0.8$  (Figure 1-24 D, G).

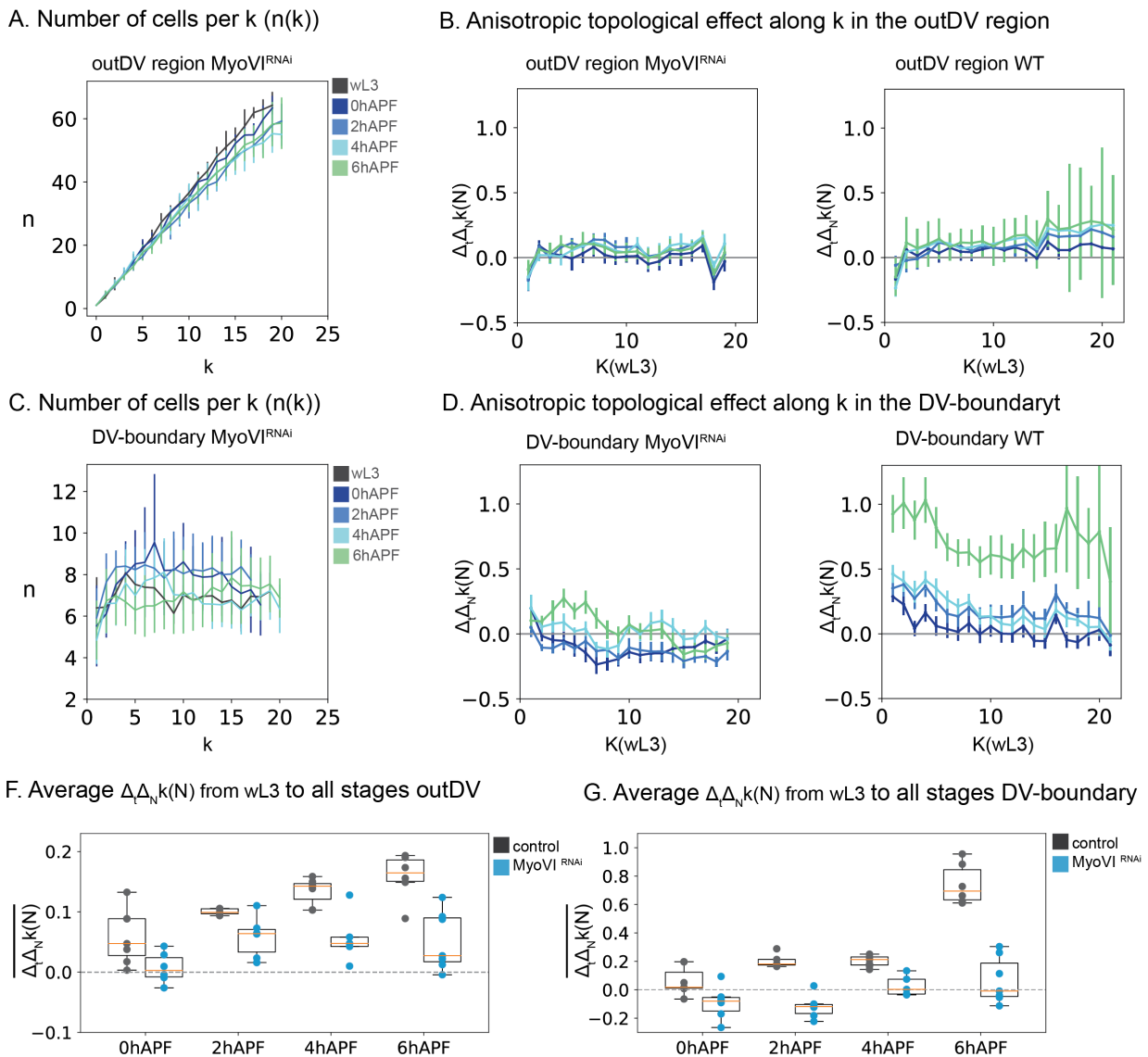


Figure 1-24 | Topological effects in  $\text{MyoVI}^{\text{RNAi}}$

Number of cells per  $k$  ( $n(k)$ ) in the outDV (A) and DV-boundary (C). Profiles for  $\Delta_t \Delta_N k(N)$  over  $K$ , where  $k(wL3)$  is used as reference. For  $\text{MyoVI}^{\text{RNAi}}$  and wildtype in outDV (B) and DV-boundary region (D). Colors correspond to the respective timepoint as indicated;  $k$  is based on  $k(wL3)$  (A-D). Error bars indicate the 95% confidence interval of the mean over all discs for each timepoint. Average  $\Delta_t \Delta_N k(N)$  for outDV (F) and DV-boundary (G). Each datapoint is one wing disc, boxplots show the median in orange, box shows upper and lower quartile values, whiskers extend 1.5 beyond upper and lower quartile. Dashed line shows no change for comparison ( $\Delta_t \Delta_N k(N) = 0$ ), wildtype in black,  $\text{MyoVI}^{\text{RNAi}}$  in blue (F, G).

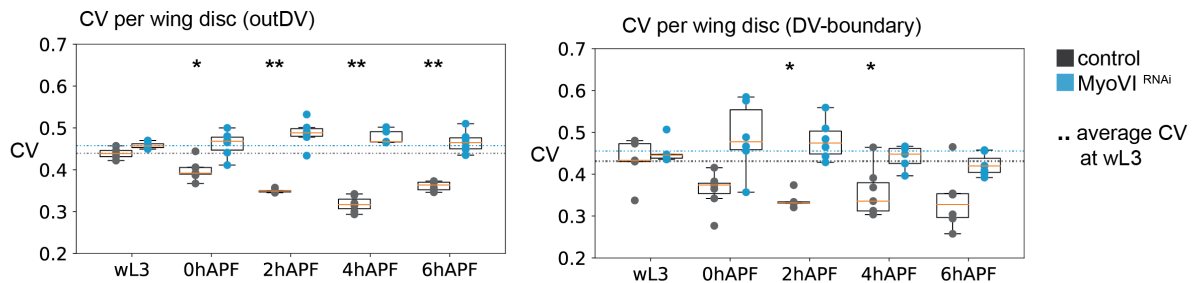
#### 1.4.5 Effects on cell packing geometry in MyosinIV knockdown wing discs

Cellular geometry and topological changes are mutually dependent (see Intro).

In Myosin knockout discs, both, area changes as well as uniaxial effect on topological rearrangements are disturbed Given our observation these observations, we addressed potential effects on cellular packing geometry. We have observed that in wildtype, cell area variability decreases and the percentage of hexagons increases over eversion. The increase in hexagons, is accounted for mostly by a decrease in pentagons and partly by a decrease in 4 and 8-sided cells (see section 1.3.1).

We do not observe a change in the coefficient of variation for cell areas (CV) in MyoVI<sup>RNAi</sup> discs as compared to wL3 (pvalues >0.05) for both regions. Indicating that cell area variability remains the same during evagination (Figure 1-25 A). We also address changes in the polygon numbers, on the 3 most common polygonal cell shapes in the tissue: 5,6 and 7. The fraction of hexagons does not change in the outDV region, during eversion, but increases at expansion. In general, the number of hexagons remains lower than in the wildtype. A similar behavior is observed in the DV-boundary, although the subtle increase in the number of hexagons is not significant. Interestingly the number of heptagons is not affected in wildtype or MyoVI<sup>RNAi</sup>, while the fraction of pentagons decreases in all conditions except for MyoVI<sup>RNAi</sup> from wL3 to 0 hAPF (Figure 1-25 B).

### A. Average cell area variability per wing disc: coefficient of variation (CV)



### B. Fraction of polygons (Pn) over time

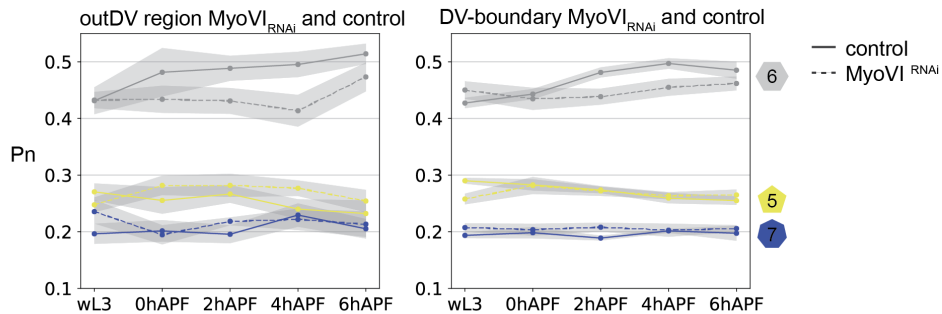


Figure 1-25 | packing geometry in *MyoVI*<sup>RNAi</sup>

Average cell area variability by coefficient of variation (CV) for outDV and the DV-boundary and *MyoVI*<sup>RNAi</sup> (blue) and wildtype (black) (A). Each datapoint is one wing disc, boxplots show the median in orange, box shows upper and lower quartile values, whiskers extend 1.5 beyond upper and lower quartile. Dotted line shows mean CV for wL3 stage for each genotype. Asterisks show statistical significance for each timepoint as compared to wL3 of the same genotype (Mann-Whitney U, two-sided, method=exact, \*\*: \*\*: 1.00e-03 < p <= 1.00e-02, \*: 1.00e-02 < p <= 5.00e-02. No asterisk: 5.00e-02 < p) (A). Fraction of polygonal cell shapes over evagination (B) Comparing the fraction of hexagons, pentagons and heptagons between wildtype (solid line) and *MyoVI*<sup>RNAi</sup> (dashed line) for outDV and DV-boundary. Shaded regions indicate the 95% confidence interval of the mean over all discs per developmental stage (B) colors correspond to polygon classes.

#### 1.4.6 Summary: Perturbation of cell and tissue shape using MyosinVI RNAi

Finish THIS

Taken together, our results indicate that MyosinVI deficient wing disc are most affected on their cell area dynamics and topological changes.

As we have seen in the wildtype, cell volume increases only a little during eversion, thus cell area expansion is coupled with cell height decrease and changes in 3D cell shape and aspect ratio. We find that in MyosinVI knockdown discs, cell volume changes are more dramatic over time. This effect is most pronounced at the end of evagination (4 hAPF).

In the outDV region, cell area changes resemble the changes in wildtype by the end of eversion. Yet the temporal dynamics are different: At the first step, from wL3 to 0 hAPF, we do not observe an area increase. Anisotropic cell area increase is then achieved at 2 and 4 hAPF, while at the same time cell volume increases. Simultaneously, in the DV-boundary, cell areas fail to increase and cell volume decreases slightly. Cell rearrangements in that region are consistently lower over all stages and cells do not elongate as much in 2 and 4 hAPF wing discs.

Another interesting observation are cell area and volume changes from 4-6 hAPF. At this transition the tissue undergoes an increase in curvature at the DV-boundary, leading to an outwards movement of the tissue margin in  $\text{MyoVI}^{\text{RNAi}}$ . This is accompanied with an increase in DV-boundary cell area and volume and a decrease in outDV cell area and volume. At the same time, we do not observe rearrangements and cells are more elongated along the DV than in wildtype. This is in contrast to the wildtype where area expansion is homogeneous throughout the tissue, cell elongation profiles resolve and rearrangements contribute to tissue-expansion.

To be included:

#### 1.5 cell division/ rearrangements in live imaging?

The role of cell divisions for eversion:

So far we have considered cell divisions as negligible although they are included in topological changes we do not consider a significant cell number increase (or decrease by death). This is motivated by work showing that cell divisions occur rarely and give rise to future neuronal progenitors and thus likely do not fulfill a role for net tissue growth.

We confirm those observations:

- AB stainings!
- How long does PH3 stain?

We employed a live imaging approach  
Can visually detect cell division in wt and myoVI  
Observe eversion in cdc2ts flies.

1.6 a role for ECM in eversion

light sheet

EM

Wing ultrastructure

The opening of the folds during eversion

